Experiments in Fluids (2026) 67:149
https://doi.org/10.1007/s00348-026-04299-8

RESEARCH ARTICLE

Wind tunnel measurements of scale effects on 3D turbulent flow in an urban street canyon configuration

Nikolaos Petros Pallas[1] · Brian Dsouza[2] · Christof Gromke[3] · Andrea Sciacchitano[2] · Demetri Bouris[1]

Received: 26 February 2026 / Revised: 10 June 2026 / Accepted: 31 July 2026

Abstract

This study examines scale effects in a wind tunnel study of an urban street canyon. A simplified modelling configuration was employed, comprising five consecutive canyons of height-to-width and length-to-width aspect ratios equal to 1 and 8, respectively, for a free-stream turbulence intensity of ~5%. Both 3D-3C Robotic Particle Tracking velocimetry and Constant Temperature Anemometry measurements were performed for Reynolds numbers exceeding the commonly accepted critical value for mean flow (~10000–20000) by a factor of ~4, i.e. ranging from 23000 to 57000. Focusing on time-averaged velocity components and turbulence kinetic energy, a novel framework is introduced to facilitate the local separation of actual Reynolds number dependence from measurement uncertainty while global indices, applied to the canyon-scale measurement volume, are implemented. Results indicate that the critical values of the Reynolds number (e.g. in the range 10000–20000) that are widely adopted in the wind tunnel testing literature may be insufficient to ensure Reynolds number independence for all examined variables and for the whole volume of urban street canyon configurations, especially near wall boundaries, as Reynolds number values up to 47000 may be necessary.

✉ Nikolaos Petros Pallas
npallas@mail.ntua.gr

[1] Laboratory for Innovative Environmental Technologies, School of Mechanical Engineering, National Technical University of Athens, 9 Iroon Polytechneiou str., 15773 Athens, Greece

[2] Flow Physics and Technology, Faculty of Aerospace Engineering, Delft University of Technology, Kluyverweg 1, 2629HS Delft, The Netherlands

[3] Laboratory of Building and Environmental Aerodynamics, Institute for Water and Environment, Karlsruhe Institute of Technology, Kaiserstrasse 12, 76131 Karlsruhe, Germany

Graphical Abstract

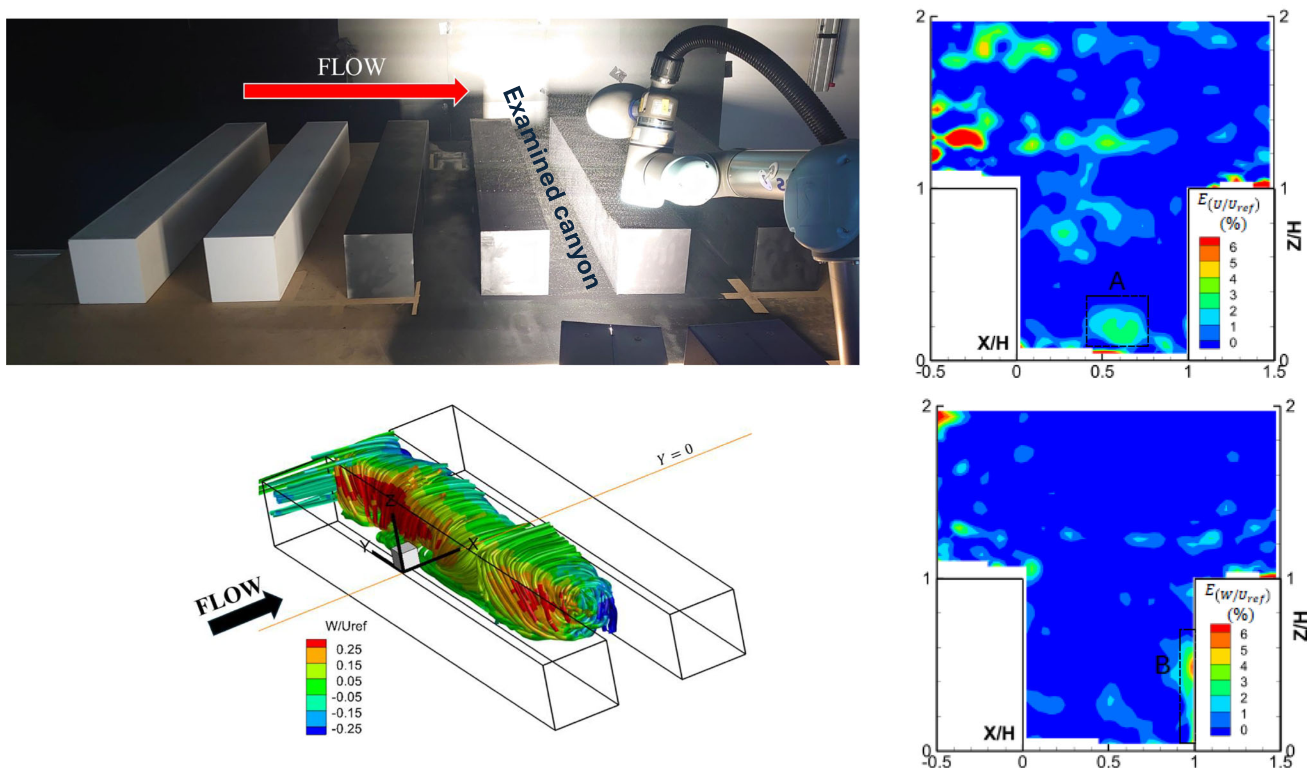

1 Introduction

The street canyon geometry, namely two adjacent rows of buildings forming a channel between them, is a fundamental part of the urban fabric. However, in many cases, it exacerbates the situation regarding pollutant (Li et al. 2006) and heat removal (Memon and Leung 2011), especially when approaching wind is perpendicular to the street canyon. This is due to a pronounced sheltering effect (Oke 1988; Jeong and Andrews 2002), i.e. less air exchange between the internal and external regions of the street canyon. The inhibition of natural ventilation, along with the fact that street canyons are encountered in every city worldwide, makes its study a fundamental part of understanding urban flow and microclimate.

Many studies of the wind environment in street canyons are performed in wind tunnels, at a laboratory scale. It is well known that in wind tunnel testing, geometric and dynamic similarity between reduced scale and full scale should be satisfied. In cases where only the time-averaged flow is of interest, the requirement of having the same Reynolds number, defined as $Re = U_{ref} H / \nu$ (with U_{ref}, H, and ν being the reference velocity, which in this case is the free-stream velocity, the characteristic length, that is, the height of the building models, and the kinematic viscosity, respectively), in the reduced-scale experiment as the one in full scale is adequate to ensure dynamic similarity. However, this requirement is most often unattainable with wind tunnel testing (American Society of Civil Engineers 2012). To achieve the full-scale Reynolds number, which is of the order of 10^6, unacceptably large geometric scales or high velocities (or both) would be required. To tackle this issue, the hypothesis of Reynolds number independence is often made. This assumption states that the flow behaviour and more specifically certain (non-dimensional) target quantities (e.g. normalised velocity fields and even higher-order velocity statistics) remain invariant beyond a critical value of the Reynolds number. The validity of the latter assumption depends not only on the target quantities but also on the specific flow that is examined (Lim et al. 2007). Fortunately, the existence of obstacles with sharp edges, which is a common feature in the urban environment, weakens the dependence of the flow behaviour on the Reynolds number, as stated by Stathopoulos and Baniotopoulos (2007). It should be noted that although Re-independence above the extracted critical Re number is frequently assumed to be valid up to the full-scale Re value, this is not always sufficiently justified, usually due to scarcity of exhaustive field measurements to be used as reference data. Quantitative differences between the two scales cannot be a priori discarded (Lim et al. 2007; Richards et al. 2001) for the whole area of interest, especially near the wall boundaries where viscous effects are predominant.

The threshold for dynamic similarity in wind tunnel studies of the flow around buildings is usually based on seminal works such as that of Castro and Robins (1977) and Uehara et al. (2003) as well as on guidelines (Snyder 1981; VDI 2000; American Society of Civil Engineers 2012). Castro and Robins (1977) have stated that, for the case of a surface-mounted cube, the value of the critical Reynolds number in a uniform flow is 30000 while in a simulated atmospheric boundary layer (ABL) flow, it reduces to 4000. For a similar case, Uehara et al. (2003) suggested a critical Re number of 3500. Furthermore, Snyder (1981) and American Society of Civil Engineers (2012) suggest a critical value of $Re = 11000$ while VDI (2000) guidelines recommend $Re = 10000$. In wind tunnel studies of street canyon configurations, Reynolds number values complying with the aforementioned limits are frequently employed (Chew et al. 2018). All the aforementioned critical values of Reynolds numbers should be interpreted and generalised with caution, since they correspond to cases of different geometry (e.g. surface-mounted cube, isolated street canyon, configuration with subsequent street canyons etc.), different approaching flows (e.g. ABL, uniform flow, etc.), and probably different surface roughness of the employed models (Snyder 1981).

An interest in examining scale effects specifically for studies of the mean flow in urban street canyon configurations has been observed in recent years. The main purpose of these studies is to determine the value of the critical Reynolds number as a guideline for wind tunnel tests involving urban street canyons. Acoustic Doppler Velocimetry (ADV) measurements were performed by Chew et al. (2018), for 7 subsequent street canyons in a water channel. They found that $Re = 12000$ ensured Reynolds number independence of the mean flow velocities and their statistics (Reynolds stresses and turbulence kinetic energy) for the case with a height-to-width aspect ratio $H/W = 1$. However, their measurements were limited to a single vertical profile, midway between the buildings that define the canyon, at the plane of flow symmetry (i.e. assuming 2D flow). Hence, the investigation of Chew et al. (2018) did not include the regions close to the canyon's walls. However, the region near the walls and the ground of a street canyon is of vital importance for pollutant dispersion studies as this is where sources or openings, determining indoor air quality, are located. This is also where relevant concentration measurements are frequently effectuated (Gromke and Ruck 2007; Gromke et al. 2008; Gromke and Ruck 2009). In a later, numerical study, Shu et al. (2020) found that $Re = 60000 - 140000$ may be required to satisfy Re-independence for the mean flow near the walls of an urban street canyon immersed in an ABL flow. Through numerical simulations, Cui et al. (2022) have also shown that the critical Reynolds number is position dependent, although they studied an isolated building equipped with openings and not a street canyon. They found that it is more difficult for the indoor flow to reach Re-independence because it is an enclosure where viscous effects are more important than in the outdoor environment. Their conclusion is in agreement with that of Shu et al. (2020) where viscous effects near walls also increased the value of the critical Reynolds number. Local variation in the critical Re number has been also mentioned by Cui et al. (2014); Lin et al. (2021); Wu et al. (2025) pertaining to studies of both isolated and urban street canyons. The canyon length-to-width (L/W) ratio also affects the critical Reynolds number along the canyon's centre plane, presumably through the differences between the bulk 2D and 3D flows that appear at different L/W values. Large-Eddy Simulation (LES) was implemented by Zhu and Chew (2025) to show that for urban street canyons with $H/W = 1$, when $L/W = 1$, the critical Re is between 8000 and 15000 while when $L/W = 4, 7, 10$ (longer canyons) Re-independence is achieved between $Re = 15000$ and 30000. Dsouza et al. (2024) also examined scale effects in both 3D (near the lateral end of the canyon) and 2D flow regions, by employing 3D–3C (i.e. 3-component) Robotic Particle Tracking Velocimetry (3D-PTV) for $H/W = 1$, when $L/W = 8$. They observed Re-independence within the range $Re = 13000, 17000$ for the mean velocities but not for the turbulence quantities. It should also be clarified that other scaling criteria besides Reynolds number similarity are mentioned in the street canyon literature (Salizzoni et al. 2011; Savory et al. 2013; Blackman et al. 2015, 2019), e.g. Jensen number similarity, similarity of integral length scales, and energy spectra of the incoming flow. However, the focus here is on Re-independence, and thus, scaling effects in the framework of this paper are solely examined with respect to the Reynolds number. Besides, the examined case consists of a simplified, quasi-2D street canyon where the approach flow is approximately uniform, and therefore, an ABL inflow, upstream of the first building, is not considered. In addition, since the examined flow is isothermal, dimensionless numbers accounting for non-isothermal effects, such as the Richardson (Ri), Grashof (Gr), and Rayleigh (Ra) numbers, are not used as a means of examining scale effects in this work.

Full-scale street canyons involve several geometrical scales and appear in numerous geometrical manifestations across different countries and cities. This introduces a significant challenge when modelling the urban environment. However, research studies have been widely implemented both experimentally (Uehara et al. 2003; Chew et al. 2018; Lin et al. 2021; Pavageau and Schatzmann 1999; Li et al. 2008; Dsouza et al. 2024; Bady et al. 2011; Kellnerová et al. 2012; Zhao et al. 2021; Xue et al. 2024b; Del Ponte et al. 2024) and numerically (Shu et al. 2020; Lin et al. 2021; Wu et al. 2025; Zhu and Chew 2025; Ai and Mak 2017; Chew and Norford 2018; Xie et al. 2007; Mirzaei and Haghighat 2011). The above-mentioned studies approach the modelling of the full-scale situation through a wide range of simplified urban street canyon configurations, including, but not limited to, a single, isolated canyon (modelling of *open country*, Meroney et al. 1996), multiple canyons (modelling of *urban roughness*, Meroney et al. 1996), different aspect ratios leading to possible 2D or quasi-2D studies, and the presence or absence of crossroads. Among those where multiple canyons are implemented, the choice varies for the number of subsequent street canyons that have been utilised. However, the underlying assumption is that the flow inside the street canyon becomes self-similar after a certain number of upstream street canyons (Chew and Norford 2018; Ai and Mak 2017). In particular, it was shown by Chew and Norford (2018); Ai and Mak (2017) that such flow self-similarity is achieved after the third subsequent street canyon. The latter assumption has been also made in the current attempt and was a posteriori supported by hot-wire measurements in selected regions.

In the context of realistically modelling a rough urban boundary layer over the examined canyon, in certain studies (Shu et al. 2020; Lin et al. 2021; Xue et al. 2024a; Pavageau and Schatzmann 1999; Bady et al. 2011) pertaining to urban street canyon configurations, an atmospheric boundary layer (ABL) was used as inflow (i.e. the approaching flow to the first building) while other research endeavours (Dsouza et al. 2024; Li et al. 2008; Ai and Mak 2017; Xie et al. 2007) relied on the flow development due to the presence of subsequent street canyons, i.e. the inflow was approximately uniform. The latter approach is adopted here, to alleviate additional complexity and facilitate future modelling and validation efforts. This may also be considered a conservative approach since previous experimental works on building aerodynamics (Castro and Robins 1977; Cheng and Fu 2010) showed that the value of the critical Reynolds number in the case of a uniform approaching flow is usually significantly higher than that obtained with an ABL inflow, i.e. even six times higher as indicated by Castro and Robins (1977). To support the assumption that the flow developed by the upstream street canyons corresponds to a rough urban boundary layer, hot-wire anemometry was used for verification.

In the present study, scale effects for an urban street canyon configuration consisting of 5 subsequent street canyons with aspect ratios $H/W = 1$ and $L/H = 8$ under perpendicular incoming wind are examined. The selected aspect ratios values guarantee the existence of skimming flow (Oke 1988; Jeong and Andrews 2002; Zajic et al. 2011), which is a common choice in street canyon studies (Gromke and Ruck 2007; Gromke et al. 2008; Gromke and Ruck 2009; Kellnerová et al. 2012; Salizzoni et al. 2009; Xue et al. 2024a) and is frequently found in cities. The choice of $L/H = 8$ ensures the development of an observable 2D flow region around the plane of symmetry (Hunter et al. 1990 suggest $L/H \geq 7$), establishing a quasi-2D flow (no crossroads are modelled). Hence, $L/H = 8$ will also allow 3D effects (manifested near the street canyon's lateral ends) to be examined. It is worth noting that subsequent experimental studies (Kastner-Klein et al. 2004; Savory et al. 2013), where the ratio L/H was a varying parameter, showed a limited but noticeable influence of L/H on the flow in the canyon centre plane even for values close to or greater than 10.

A 3D-3C Robotic PTV system is implemented to study scale effects for the time-averaged flow in the vicinity of the fourth street canyon. The PTV experimental method enables the investigation of Reynolds number independence across a large measurement volume containing approximately half the canyon. Furthermore, the employment of PTV allows systematic investigation of scale effects, either locally or by applying global, data reduction metrics. The latter canyon-scale metrics facilitate the identification of regions which are susceptible to Reynolds number dependence across the whole examined volume. The above-mentioned investigative tools are applied to both time-averaged velocity and turbulence kinetic energy. An important part of the current attempt is the quantification of the uncertainty, in order to distinguish between measurement noise and actual scale effects. Finally, following previous works (Chew et al. 2018; Dsouza et al. 2024), the present study examines a range of Reynolds number values, achievable in a typical wind tunnel (i.e. $23000 \leq Re \leq 57000$) and aims to complement existing data and experimentally investigate the suggestion of locally varying Reynolds number independence which has been introduced through older numerical studies (Shu et al. 2020; Cui et al. 2022). It is noted that the maximum examined Re number is larger than the commonly accepted one (Snyder 1981; VDI 2000; American Society of Civil Engineers 2012) by a factor of ∼4. To the best of the authors' knowledge, this is the second time (Dsouza et al. 2024) that 3D-PTV is applied to a street canyon configuration. However, the investigation herein is performed for a range of higher Reynolds numbers and an inflow of higher ambient turbulence levels, which is more representative of a rough urban environment. In summary, the distinct goals of the current study read as follows:

- Apply state-of-the-art measurement techniques (i.e. PTV) to evaluate localised Re-independence throughout the canyon volume. This is highly relevant for applications that may depend on flow variables (mean velocity and turbulence kinetic energy) and flow characteristics (2D or 3D) in close proximity to wall boundaries. The underlying conclusions provide new insights regarding the frequent assumption of dynamic similarity in wind tunnel testing of flow in simplified models of urban street canyons.

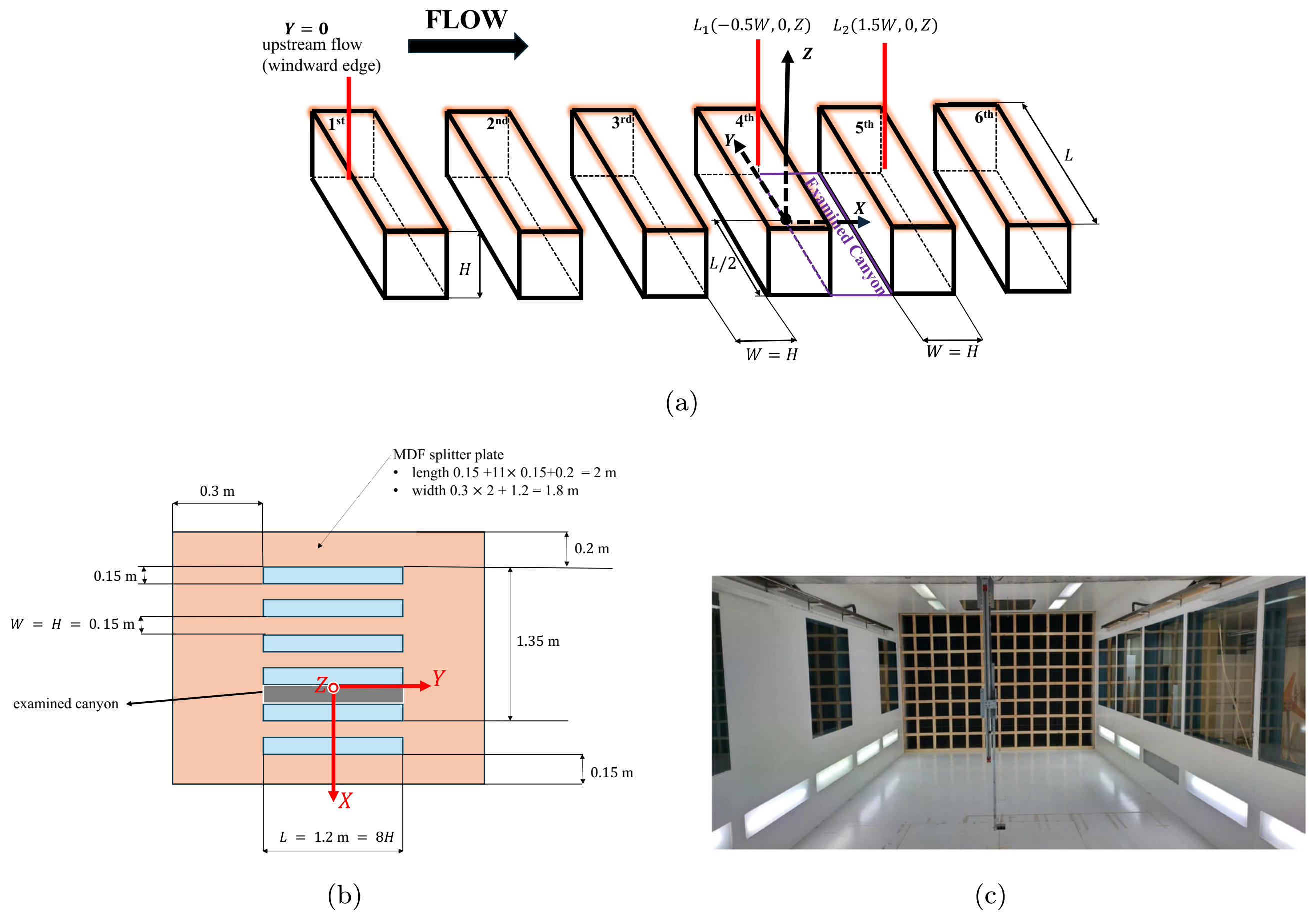

Fig. 1 Schematic illustration of: **(a)** the model (3D view), its orientation with respect to the approaching flow and its coordinate system. Hot-wire measurement positions are indicated as red lines. **(b)** The model (top view) along with some structural details. The examined canyon is indicated in both figures. **(c)** The employed passive grid responsible for increasing the free-stream ambient turbulence

- Create a framework where quantification of uncertainty is an integral part of the assessment of scale effects along with global (i.e. canyon-scale) indices. The developed analytical and investigative tools comprising this framework are generalisable and could be applicable to other cases where the investigation of scale effects is the primary target.

Conclusions derived from the examined “canonical”/simplified form of an urban street canyon will hopefully provide a basis for future studies in similar configurations that could include more geometric detail and may also examine the effects of variants in the inlet conditions (i.e. approaching flow). It should be clarified that although the focus of this study is on Reynolds number effects, the potentially obtainable information from the examined data set is by no means limited to this scope; for example, other research directions could pertain to air ventilation (Blackman et al. 2015; Chew and Norford 2018), a deeper investigation of the spanwise turbulence statistics (Jaroslawski et al. 2019), or even data assimilation (Suzuki et al. 2009).

2 Methodology

2.1 Model setup

The model setup was an urban street canyon configuration consisting of 5 subsequent street canyons with aspect ratios $H/W = 1$ and $L/H = 8$. Scale effects were investigated in the vicinity of the fourth canyon (examined canyon). The coordinate system, the basic dimensions of the model, as well as its orientation with respect to the approaching flow are shown in Fig. 1a. The axes X, Y, Z correspond to the streamwise, lateral, and ground-normal (vertical) directions, respectively. Hot-wire measurement positions are also indicated as red lines.

A top view of the model and its layout is given in Fig. 1b. A splitter plate was used to elevate the model from the ground, eliminating boundary layer effects originating from the floor of the wind tunnel. The leading edge of the splitter plate was shaped to form an angle of $\sim 40°$ to reduce the effect of the plate's stagnation region.

The cross section of the closed-loop wind tunnel facility of the National Technical University of Athens (NTUA) is 2.5m $\times$ 3.5m. This yields a model blockage ratio $\sim 6.5\%$. The free-stream turbulence intensity is $\sim 5\%$, achieved by applying a square-mesh (Roach 1987) passive turbulence grid to the inlet of the test section (Fig. 1c). The grid consisted of wooden bars with a cross section of $l \times d = 24\,\text{mm} \times 48\,\text{mm}$, where d is the width (dimension normal to the flow). The distance between the centres of the bars was $M = 30\,\text{cm}$. This grid geometry yields a porosity equal to $\beta = (1 - d/M)^2 = 0.7$, which is a typical value for passive grids (Kistler and Vrebalovich 1966; Roach 1987; Vita et al. 2018). This passive grid had been constructed and used in the framework of a Round-Robin test focusing on wake measurements of porous discs (Hölling et al. 2025). The reported free-stream turbulence intensity had been measured as part of the previously mentioned experimental campaign, above the region of the test section onto which the street canyon models were installed. As far as the decay of the grid-generated turbulence is concerned, it was found that it decreases from a value of 7% at 3 m ($10M$) downstream of the inlet of the test section (see Table 1 of Hölling et al. 2025) to 5% above the region of interest, i.e. where the canyons were installed, namely $\sim$8 m ($\sim 27M$) from the inlet of the test section. These values have been acquired by means of hot-wire anemometry, and more details about these measurements can be found in (Hölling et al. 2025). Regarding the dependence on the Reynolds number of the flow induced by the passive grid, only minor Reynolds number effects were observed by Hölling et al. (2025) when a passive grid of the same mesh size ($M = 30$ cm) and bar width ($d = 4.8$ cm) was utilised. It should be clarified though that this conclusion is only limitedly applicable to the present case, as it was extracted for $Re > 60000$ and for different wind tunnel facilities. The classic study of Roach (1987) indicates that square-mesh arrays of square bars are Re-insensitive with respect to the pressure losses and the streamwise turbulence intensity induced by the passive grid as well as the downstream decay of the latter, over the range $Re_d \in (100, 10000)$, where $Re_d = d \cdot U_{ref}/\nu$. With the current Re_d being in the range (7000, 18000), there is only a partial overlap with the Re_d range examined by Roach (1987). In addition, the bars of the employed passive grid are of rectangular cross section and not square. For the previous reasons, combined with the fact that the results of Roach (1987) may not be valid for every wind tunnel facility (Vita et al. 2018), a brief discussion for this matter—at least with respect to the streamwise velocity and turbulence intensity—is included in Subsect. 3.1.

2.2 Examined cases

In the current investigation, two different measurement techniques have been employed: Robotic Particle Tracking Velocimetry (PTV) and Constant Temperature Anemometry (CTA) with a hot-film (HF) probe. The tested Reynolds numbers for both measurement techniques were $Re =$ 23000, 28000, 37000, 47000, and 57000. A maximum mismatch of 2.6% is observed between Reynolds numbers (Re) of HF and PTV measurements per examined case. The data are openly accessible at (Pallas et al. 2025).

The following should be noted/reminded: (a) the Reynolds number is defined as $Re = U_{ref}H/\nu$, where U_{ref} is the free-stream velocity, H is the height of the building models, and ν is the kinematic viscosity of the air. (b) Hot-wire measurements were performed in order to quantify the flow exactly upstream and above the first building as well as at the middle of the roof of the fourth and fifth building (red lines of Fig. 1a). The latter velocity profiles were measured to quantify the developing boundary layer due to the presence of the subsequent street canyons and to examine if it is sensitive to the Re number. All velocity profiles are measured on the symmetry plane ($Y = 0$). (c) The PTV measurements spanned a volume containing more than one half of the street canyon, reaching up to 2 heights above the roofs of the buildings.

2.3 Measurement system

The basic component of the PTV measurement system is the Coaxial Volumetric Velocimetry (CVV) probe (Schneiders et al. 2018), consisting of four CMOS cameras which are enclosed in an aerodynamic shell (LaVision Minishaker Aero). This probe, which is shown in Fig. 2, is mounted on a Universal Robots UR5 robotic arm with translation accuracy equal to 0.1 mm (Jux et al. 2018). The focal length and numerical aperture of the mounted camera system are 4.1 mm and 11, respectively, resulting in a magnification factor of 0.008. The system was provided by TU Delft.

Although the maximum sampling frequency (f_{acq}) of the system is 727Hz, its actual value was adjusted, depending on the Reynolds number, to ensure that the particle image displacement did not exceed 15 pixels at the given free-stream velocity. Other acquisition parameters (see the following equations) were then adjusted to achieve at least 78 vortex turnovers (considered to be equivalent to the number of independent samples). Although it was shown by Ahn and Fessler (2003) that even a number greater than 10 ($N_t > 10$) was adequate to ensure statistically converged calculations of standard uncertainty, it should be noted that the number of independent samples required to ensure statistical convergence is case dependent. Here, judging by the statistical error (Subsect. 3.3), the acquisition of $N_t = 78$ canyon vortex rotations is considered adequate. A priori estimation of

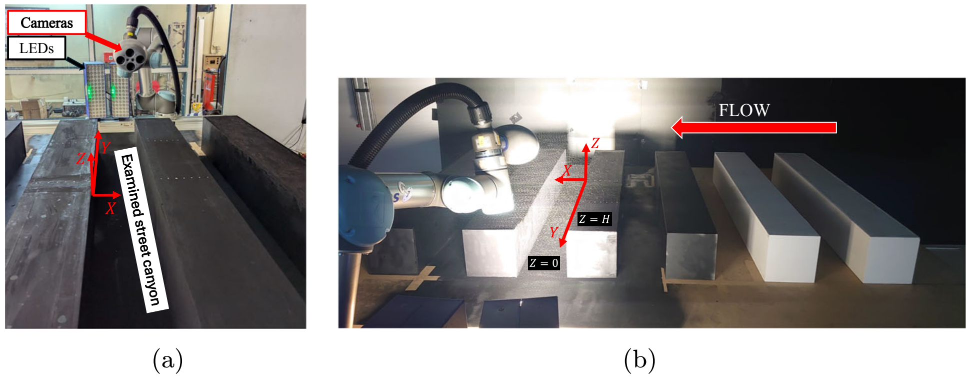

Fig. 2 **(a)** Measurement system using the Coaxial Volumetric Velocimetry (CVV) probe (Schneiders et al. 2018) mounted on a Universal Robots UR5 robotic arm. The whole system is installed inside the test section of NTUA. **(b)** The same system in working mode. The presence of seeding as well as the whole model is also discernible

the number of captured vortex turnovers was based on the following assumption (Gromke and Ruck 2009):

$$U_c = 0.3 U_{ref} \tag{1}$$

where U_c is an estimate of the circumferential velocity of the canyon vortex and U_{ref} is the reference velocity corresponding to the undisturbed flow. The vortex turnover time is then calculated according to the following equation:

$$T_t = \frac{\pi H}{U_c} \tag{2}$$

with H being the height of the canyon (also equal to the width W). Finally, the following relation is used, where $a = 5$ (number of individual acquisitions) with at least $N_{im} = 3000$ images captured per acquisition:

$$N_t = a\frac{T_{\text{acq}}}{T_t} = a\frac{N_{im}}{T_t \cdot f_{acq}} \geq 78 \tag{3}$$

Helium-filled soap bubbles (HFSB) (Faleiros et al. 2019) of 300 μm median diameter (Kim et al. 2020) were used as tracer particles for PTV. It has been proved in the past (Scarano et al. 2015; Faleiros et al. 2018, 2019) that the bubbles have a particle response time ranging from 11 μs to 42 μs, depending on the helium flow rate. By applying the same reasoning as in Scarano et al. (2015), the characteristic flow time scale is estimated as $H/U_{ref} = 2 \times 10^4$ μs (U_{ref} at $Re = 57000$). Consequently, since there is a difference on the order of 10^4 between the particle and the flow time scales, HFSB is considered a suitable choice to seed the examined flow. Regarding the performance of the HFSB as a seeding material near wall boundaries, Faleiros et al. (2018) concluded that the mean velocity and the turbulent fluctuations of turbulent boundary layers above a distance of approximately two bubble diameters (< 1mm) from the wall can be reliably measured. The seeding particles are discernible in Fig. 2b.

The use of LEDs for illumination instead of lasers is feasible due to the relatively large size of the HFSB which leads to more light being scattered in comparison with more conventional seeding materials, e.g. oil droplets (Raffel et al. 2018). Two LaVision LED Flashlight 300 s were utilised to obtain sufficient pulsed volumetric illumination (Fig. 2). The LEDs have an operating angle of 10° and a maximum frequency of 20kHz while they can be used in continuous or pulsed mode.

Regarding the processing of the PTV raw data, the following workflow is implemented: (i) pre-processing, i.e. removal of the background noise via subtraction of the time minimum pixel intensity on a slide kernel of 5 or 7 images, (ii) processing: the Shake-The-Box (STB) algorithm (Schanz et al. 2013, 2016) is used to identify particle tracks, (iii) post-processing consisting of outliers' detection and filtering of the tracks, and (iv) binning (Agüera et al. 2016), i.e. ensemble averaging of particle tracks within sub-volumes of user-defined size, i.e. $19 \times 19 \times 19$ mm^3 with an overlap factor of 75% between bins, resulting in a vector pitch of 4.75 mm. In this way, a description of the time-averaged velocities on an Eulerian frame as well as the respective standard deviations is provided. Values of the standard measurement uncertainty are reported in Subsect. 3.3.

Hot-wire anemometry is employed in order to obtain high-frequency velocity measurements of the background flow (upstream and above the canyon). A TSI IFA 300 measurement system with a single hot-film (HF) Model 1201 TSI probe was utilised. The sampling frequency and the time of acquisition/averaging were 1kHz and 65 s, respectively. The HF measurement error is generally 3–5% of the free-stream velocity. A detailed calculation of the HF measurement error is included in Appendix, which provides the data for the error bars in the figures containing HF results (Figs. 3 and 4).

During the experiments, the free-stream velocity was monitored in the undisturbed flow region with a Pitot-static tube connected to a FCO432 differential pressure transmitter (Furness Controls Ltd, ±150 Pa, uncertainty: from 0.075 Pa when the measured pressure is 0.21 Pa to 1.4 Pa when the measured pressure is 37 Pa, at 27 − 28 °C). A Pt100 thermometer (range 0 − 50°C, accuracy 0.0236°C) was used for measuring the temperature inside the test section.

Fig. 3 Profiles at the windward edge of the first building (see Fig. 1a) for: **(a)** the time-averaged, non-dimensional velocity U/U_{ref} and **(b)** $\sqrt{\overline{u'^2}}/U$ where u' is the streamwise velocity fluctuation. The results are shown for the minimum and maximum Reynolds numbers, i.e. $Re = 23000$ and $Re = 57000$, respectively

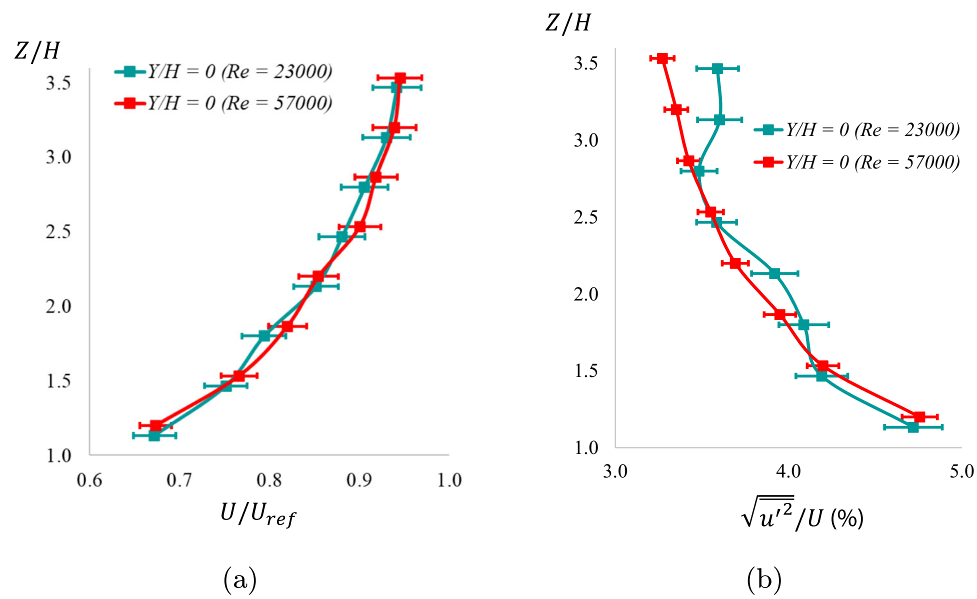

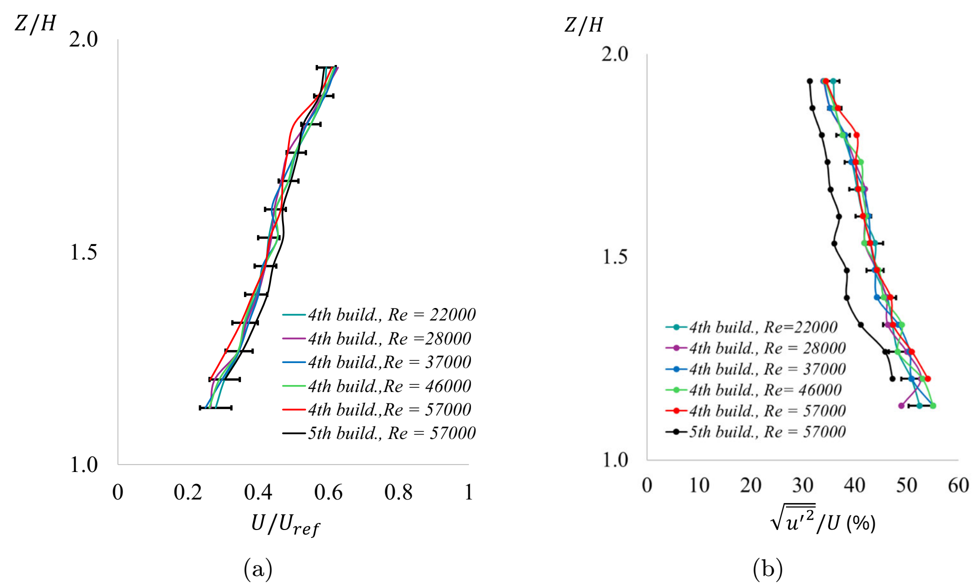

Fig. 4 **(a)** Time-averaged non-dimensional (streamwise) velocity U/U_{ref} and **(b)** $\sqrt{\overline{u'^2}}/U$, where u' is the streamwise velocity fluctuation, along the lines L_1 ($X/H = -0.5$, $Y/H = 0$, Z), L_2 ($X/H = -1.5$, $Y/H = 0$, Z), located at the centre of the roofs of the 4th and 5th buildings, respectively. Results are given for 5 different Reynolds numbers in the range $Re \in [23000, 57000]$ for line L_1 and at $Re = 57000$ for line L_2. Both lines are shown in Fig. 1a

2.4 Metrics and uncertainty

The equations presented in this section are used to assess the non-dimensional differences between individual Reynolds numbers while quantifying the uncertainty of the examined results. The ultimate goal is to combine both the above-mentioned concepts in a unified framework, which can be then used to provide a robust and reliable analysis of scale effects. Under this rationale, the following equation is initially introduced to quantify the difference in a measured quantity at different Re numbers:

$$|\Delta Q| = \left| Q_{Re_I} - Q_{Re_J} \right| \tag{4}$$

with Q being $\overline{U}/U_{ref}$, $\overline{V}/U_{ref}$, $\overline{W}/U_{ref}$ or k/U_{ref}^2 and Re_I, $Re_J = 23000, \ldots 57000$, $I \neq J$. $\overline{U}$, $\overline{V}$, and $\overline{W}$ are the time-averaged streamwise, lateral, and vertical velocity components, whereas k is the turbulence kinetic energy. From now on, the overbar is omitted for brevity. Equation (4) is applied to any measurement point for any variable Q.

From uncertainty propagation, the following equation is derived for the uncertainty of Eq. (4):

$$\epsilon_{|\Delta Q|} = \sqrt{\epsilon^2_{Q_{Re_I}} + \epsilon^2_{Q_{Re_J}}} \tag{5}$$

where $\epsilon_{Q_{Re_I}}$, $\epsilon_{Q_{Re_J}}$ correspond to the uncertainty at Re_I, Re_J, respectively. The latter two variables are considered uncorrelated for the derivation of Eq. (5).

In the current attempt, it is assumed that the finite sample size (Sciacchitano and Wieneke 2016) is the dominant source of uncertainty of the examined statistical quantities. However, apart from the above-mentioned statistical error, there are, of course, other sources of systematic error, such as:

- Calibration error. Even with a careful geometric calibration, remaining errors in the range of 0.5–2 pixel can still be present (Wieneke 2008). With 3D PTV, where triangulation of individual particles is implemented, these errors can be significant. For this reason, volume-self calibration (Wieneke 2008) was applied throughout the processing of the presented cases, which reduced calibration errors to below 0.1 pixel. Since the particle image displacement did not exceed 15 pixels at the given free-stream velocity, this means that the remaining calibration error was $\sim 0.1/15 = 0.7\%$ of the reference velocity. Therefore, the systematic error due to imperfect calibration is not considered a crucial source of uncertainty in the current attempt.
- Interpolation of the initial particle tracking velocimetry data onto a grid. According to Schneiders and Sciacchitano (2017), an interpolation technique may introduce errors that are not inherent to the particle tracking measurements, such as a bias due to imposition of a boundary or an incompressibility assumption and/or due to limited seeding concentration. No incompressibility assumption or imposition of a boundary has been made here. Furthermore, the seeding concentration is considered adequate since the spatially averaged number of particles (ensemble members) per bin is above 10^4 for all examined Re numbers. Therefore, the interpolation error is not considered an important source of systematic error here. It should be noted though that locally, namely in regions of low seeding concentration, it can be significant.
- As explained by Jux et al. (2018), the presence of the robot in the flow may cause some bias of the velocity because of local flow accelerations. However, Jux et al. (2018) found that a velocity disturbance $\leq 1\%$ is observed whenever the distance between the probe and the examined area is larger than or equal to 17.5 cm. The former requirement was always respected throughout the conducted experiments.

Two remarks should be made with respect to the previous discussion of systematic errors in PTV: (a) an attempt was made to assess the main sources of systematic error in PTV measurements that are relevant to the examined case and readily quantifiable. However, the above list of errors should not be considered as an exhaustive enumeration of all potential systematic errors reported in the literature (Timmins et al. 2012; Sciacchitano 2019; Bhattacharya and Vlachos 2020). (b) Although the uncertainty due to the finite sample size (see Subsect. 3.3 for quantification) is generally more important than the one linked to the above-listed sources of errors for the examined case, ignoring the latter while performing uncertainty quantification inevitably leads to an underestimation of the true measurement uncertainty. This is not considered detrimental for the purposes of this study since an underestimation of the uncertainty will lead to a less conservative evaluation of Re-dependence where more regions are identified as potentially dominated by scale effects. In this study, an additional step is undertaken to exclude regions that are not actually dominated by scale effects but are instead artefacts originating from an underestimation of the uncertainty. This consists of localised comparisons, i.e. by means of line plots and contours. Conversely, an overestimation of the uncertainty would inhibit the method's ability to identify regions susceptible to scale effects, since discrepancies between different Reynolds numbers would be attributed to uncertainty and not to the actual Reynolds number effects. Owing to the fact that only differences between two compared Re numbers that exceed the underlying uncertainty are attributed to scale effects, the uncertainty can be viewed as a threshold separating the occurrence of Reynolds number independence from scale effects (Re-dependence).

The standard uncertainty, linked to the finite sample size, for time-averaged quantities, ϵ_Q with Q being U/U_{ref}, V/U_{ref} or W/U_{ref} is calculated as (Sciacchitano and Wieneke 2016):

$$\epsilon_Q = \frac{\sigma_Q}{\sqrt{N}} \tag{6}$$

where σ_Q and N are the standard deviation and the number of independent samples, respectively.

The assumption that every vortex turnover constitutes an independent flow event, and, therefore, it can be viewed as uncorrelated with any other such independent event, has been made in this study. Therefore, N is always considered equal to the number of the (processed) vortex turnovers, N_t (see Eq. 3). The option of increasing the number of acquisitions (per tested Re number) and then using them as independent samples for the purpose of uncertainty quantification was not a realistic choice due to potentially prohibitive memory storage and processing time requirements.

For the turbulence kinetic energy (TKE), i.e. $Q = k/U_{ref}^2 = 0.5(\overline{u'u'} + \overline{v'v'} + \overline{w'w'})/U_{ref}^2$, the following expression is used (Sciacchitano and Wieneke 2016):

$$\epsilon_{\overline{u_i'u_i'}} = \sigma_{U_i}^2 \cdot \sqrt{\frac{2}{N}} \tag{7}$$

where $\sigma_{U_i}^2$ is the variance of the corresponding velocity component. From uncertainty propagation, the following equation is extracted:

$$\epsilon_{(k/U_{ref}^2)} = \sqrt{\frac{1}{2N}} \cdot \sqrt{\sigma_{U/U_{ref}}^4 + \sigma_{V/U_{ref}}^4 + \sigma_{W/U_{ref}}^4} \tag{8}$$

where the covariances of velocity components are assumed to be negligible.

As a clarification of the statistical meaning of the already described framework, it is stated that if the difference $|\Delta Q|$ (Eq. 4) follows a distribution, e.g. Gaussian, then $\epsilon_{|\Delta Q|}$ (Eq. 5) is its standard deviation. In essence, the quantity $\epsilon_{|\Delta Q|}$ functions as a means of quantifying the uncertainty of the difference $|\Delta Q|$, i.e. $|\Delta Q| \pm \epsilon_{|\Delta Q|}$. Based on the previous reasoning, the following equation is introduced:

$$E_Q = |\Delta Q| - \epsilon_{|\Delta Q|} \tag{9}$$

where E_Q will be called *net difference* from now on. It quantifies the importance of $|\Delta Q|$ with respect to $\epsilon_{|\Delta Q|}$, revealing regions of high E_Q values potentially dominated by scale effects.

Equation (9) is viewed as a conservative metric of the difference of Q between two compared Re numbers since it accounts for the standard measurement uncertainty. On the other hand, $|\Delta Q| + \epsilon_{|\Delta Q|}$ would essentially lead to an inflated value of the difference between two examined Re numbers, since the standard measurement uncertainty would be considered as a contributing factor to the latter difference. E_Q functions as a marker of potentially Re-dependent regions. The difference $|\Delta Q| - \epsilon_{|\Delta Q|}$ is used instead of the ratio $|\Delta Q|/\epsilon_{|\Delta Q|}$ as very small values of uncertainty in the denominator would skew the results. If $E_Q > 0$, then these regions are potentially dominated by scale effects with larger values indicating more pronounced scale effects. Negative values of E_Q indicate that the standard measurement uncertainty is too high to extract any conclusions regarding Re-sensitivity so they are shown as zero throughout the analysis presented in the following sections. Regions with marginally positive E_Q and high uncertainty $\epsilon_{|\Delta Q|}$ should be interpreted with care and by using complementary investigative tools, e.g. comparison of velocity and/or turbulence kinetic energy profiles between different Re numbers, pertaining to these regions.

Apart from the above-presented quantification of the uncertainty due to the finite sample size, some indicative, canyon-scale results for the instantaneous uncertainty are also provided in Sect. 3.3. It should be emphasised though that since the focus here is on statistical quantities (time-averaged velocities and turbulence kinetic energy), this type of uncertainty is not explicitly included in the net difference metric previously introduced in Eq. (9). The instantaneous uncertainty prior to binning (i.e. ensemble-averaging) is calculated through DaVis software of LaVision. The latter calculation is based on the work of Janke and Michaelis (2021), who considered the particle positions reconstructed along a trajectory, fitted a certain polynomial of a given degree and a given kernel size, computed the residual between the measured particle positions and the fitted polynomial, and finally propagated that residual to the velocity. This approach accounts only for random errors and does not consider any systematic uncertainties arising from the polynomial fitting. Moreover, it may underestimate the overall uncertainty when a substantial number of outliers (e.g. tracks resulting from reflections) are present in the acquired data, as these are not taken into account. However, outliers are usually removed prior to binning through appropriate filtering. This instantaneous uncertainty is denoted as ϵ_{pb}, where pb corresponds to *prior binning*. Since ϵ_{pb} is calculated along every track, a histogram is finally produced. To extract a representative value from this histogram, the following procedure is applied for every Re number and every measured velocity component, separately:

1. The uncertainty value $\epsilon_{pb,97.5\%}$ (in m/s) is defined. This is feasible by finding the range $[0, \epsilon_{pb,97.5\%}]$ within which 97.5% of the entire measurement set (i.e. ensemble of tracks) falls with respect to the calculated uncertainty ϵ_{pb}. The value of $\epsilon_{pb,97.5\%}$ is found for every acquisition (see Eq. 3).
2. Then, the non-dimensional, acquisition-averaged value $\langle \epsilon_{pb,97.5\%} \rangle / U_{ref}$ (%) is calculated.

In addition to the previously established framework based on the net difference metric (Eq. 9), which primarily focuses on local (point-wise) investigation of Reynolds number independence, global (canyon-scale) investigative tools and metrics are also employed. In this scope, the correlation coefficient (Rotello et al. 2025) between quantities at $Re = Re_{max}$ and $Re \neq Re_{max}$ is introduced:

$$R = \frac{\sum_{j=1}^{n}(x_j - \langle x \rangle)(y_j - \langle y \rangle)}{\sqrt{\sum_{j=1}^{n}(x_j - \langle x \rangle)^2 \sum_{j=1}^{n}(y_j - \langle y \rangle)^2}} \tag{10}$$

where x and y correspond to the normalised variables (i.e. U/U_{ref}, V/U_{ref}, W/U_{ref} or k/U_{ref}^2) at $Re \neq Re_{max}$ and $Re_{max} = 57000$, respectively. The angled brackets $\langle\cdot\rangle$ correspond to the spatially averaged value across the whole volume and n is the number of measurement points within this volume.

As a means of quantifying the spread around the $y = x$ line, the equation of the mean square error MSE is employed:

$$\mathrm{MSE} = \frac{1}{n}\sum_{j=1}^{n}(y_j - x_j)^2 \tag{11}$$

A normalised version of MSE, i.e. MSE^*, is the following:

$$\mathrm{MSE}^* = \frac{\mathrm{MSE}}{\Delta y_{95\%}^2} \tag{12}$$

with $\Delta y_{95\%}^2$ being the range of the variable $y = U/U_{\mathrm{ref}}$, V/U_{ref}, W/U_{ref} or k/U_{ref}^2 (at $Re = 57000$) within which 95% of the total number of measurements fall. This enables comparisons between variables. The threshold 95% was used instead of 100% for the sake of outliers' exclusion.

As already mentioned in Subsect. 2.2, the Reynolds number is $Re = U_{ref}H/\nu$ with $\nu = \mu/\rho$, where μ and ρ are the dynamic viscosity and the density, respectively. The dynamic viscosity can be calculated as a function of the temperature through Sutherland's formula (White 2006) which is found in Appendix. By disregarding the uncertainty in the reference length, H, and by considering μ, ρ and U_{ref} uncorrelated, the equation, quantifying the uncertainty of Re, reads as follows:

$$\epsilon_{Re} = \sqrt{\left(\frac{\partial Re}{\partial \mu}\right)^2 \cdot \epsilon_\mu^2 + \left(\frac{\partial Re}{\partial \rho}\right)^2 \cdot \epsilon_\rho^2 + \left(\frac{\partial Re}{\partial U_{ref}}\right)^2 \cdot \epsilon_{U_{ref}}^2} \tag{13}$$

Such uncertainty is below 3.5% in the examined range of Re numbers. More details pertaining to the aforementioned calculation are given in the next section while a complete quantification of the uncertainties ϵ_μ, ϵ_ρ and $\epsilon_{U_{ref}}$ as well as the derivatives participating in Eq. (13) is found in the Appendix.

Regarding the uncertainty of hot-film measurements, three main sources of error are considered here: (a) the error of the calibrator (FCO432 differential pressure transmitter), (b) the curve fitting error, ϵ_{ft} (here at most ~2%) and (c) the statistical error, ϵ_{st}. The first two sources of uncertainty are stated as two of the most important by Jørgensen (2001) during the stage of acquiring and converting the voltage signal to a velocity sample. The uncertainty due to temperature difference (Jørgensen 2001) between the calibration and the actual measurements is considered negligible since temperature compensation was always applied during the measurements. Finally, the following equation is applied to quantify the total error of the HF measurements:

$$\epsilon_{HF} = \sqrt{\epsilon_{U_{clb}}^2 + \epsilon_{ft}^2 + \epsilon_{st}^2} \tag{14}$$

More details about the error of the hot-film measurements are found in Appendix.

3 Results and discussion

3.1 Flow structure upstream and above the canyon

Hot-film measurements were performed at the upper windward edge of the model (as shown in Fig. 1a) in order to quantify both the time-averaged streamwise velocity and streamwise turbulence intensity. The results are shown in Fig. 3 for the minimum and maximum Reynolds numbers, i.e. 23000 and 57000, respectively. Error bars corresponding to the hot-film error (see Eq. 14 and Appendix) are also included for both the minimum and maximum Reynolds numbers. The span of the latter is generally less than that of the former, with the main reason being the lower levels of standard uncertainty due to the higher number of independent samples (i.e. smaller time scales T_I, see Eq. 19 of Appendix). Reynolds number independence is generally observed for both the streamwise velocity and the streamwise turbulence intensity although some small differences, i.e. $\left|\Delta\left(\sqrt{u'^2}/U\right)\right| = \left|\left(\sqrt{u'^2}/U\right)_{Re=57000} - \left(\sqrt{u'^2}/U\right)_{Re=23000}\right| = 0.32\%$ of U (i.e. the streamwise velocity at an examined height, Z/H) at most, are observed for the latter, probably due to imperfect statistical convergence. For the velocity, the difference is at most 2% of U_{ref}. For the calculation of the above-mentioned differences, linear interpolation has been applied due to a slight height shift (i.e. a shift along the Z axis) equal to $0.067H$ of the curve at $Re = 57000$ compared to that at $Re = 23000$. The flow exactly upstream and above the first building presents small velocity differences between the minimum and the maximum Re numbers, indicating negligible influence of other parameters, e.g. the passive grid applied at the inlet of the test section, with respect to scale effects. The velocity ranges from $0.7U_{ref}$ to U_{ref} while the streamwise turbulence intensity near the roof of the first building is close to 5%.

Further details of the flow surrounding the examined canyon are as follows: (i) regarding the lateral uniformity of the approaching flow at the leading edge of the splitter plate (although the precise position is subject to spatial limitations imposed by the measurement equipment), the relative differ-

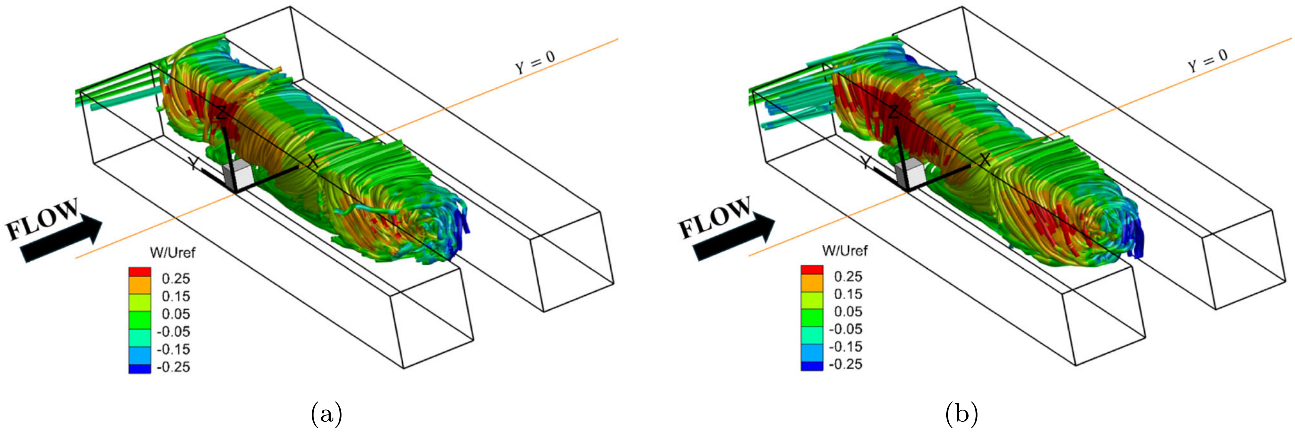

Fig. 5 Stream traces coloured with the values of the time-averaged vertical velocity W/U_{ref} for: **(a)** $Re = 23000$ and **(b)** $Re = 57000$

Fig. 6 **(a)** Global uncertainty metric $\langle \epsilon_{pb,97.5\%} \rangle / U_{ref} (\%)$ shown for $Re = 23000$ to 57000, for all the velocity components. **(b)** Standard uncertainty profiles at $X/H = 0.5$ and $Y/H = 0$, i.e. midway between the buildings on the canyon's centre plane, for $Re = 23000$ and $Re = 57000$ and for the streamwise and the vertical velocity

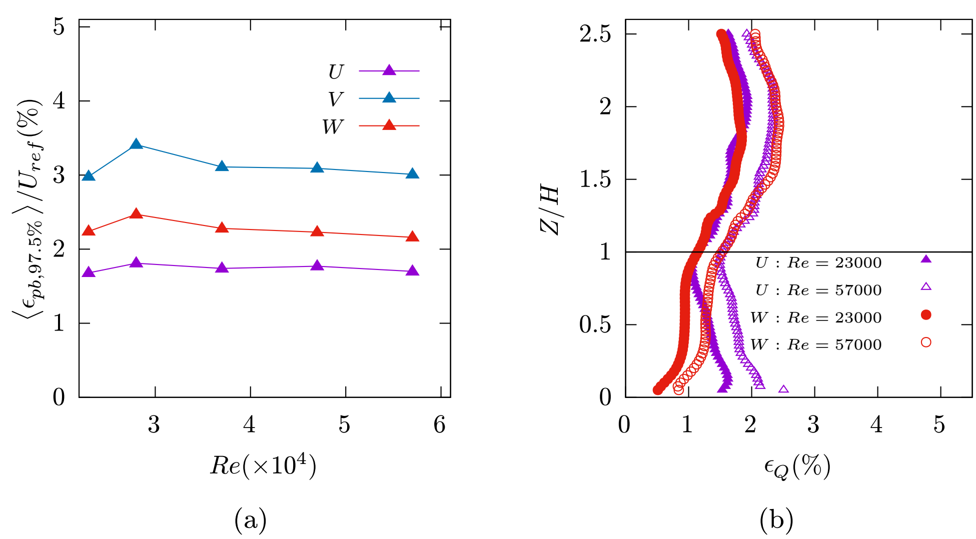

ence of the time-averaged velocity between the left and right side of the whole model (i.e. at $Y \pm L/2$, see Fig. 1) ranges from 4 to 7% for $0 \leq Z/H \leq 2$. These differences were calculated after measurements with a Pitot-static tube mounted on a traverse system. (ii) Hot-film (HF) velocity measurements (at $Re = 57000$) up to $Z/H \sim 2$ and in the middle of the roofs of the fourth and fifth building (see Fig. 1a) established that the time-averaged velocity difference was at most 6% of the reference velocity and that the streamwise turbulence intensity differed by less than 8% in the same region. This comparison is shown in Fig. 4 along with measurements at different Re numbers in the middle of the roof of the fourth building. It is interesting to note that the velocity differences between the profiles on the fourth and fifth roofs—both at $Re = 57000$—are generally within the margins defined by the error bars. These error bars correspond to the hot-film measurement error (see Eq. 14 and Appendix) and are included only at $Re = 23000$ for the sake of visibility. In conclusion, the underlying assumption that the flow inside the street canyon becomes approximately invariant (i.e. differences remain within the error margins) after three upstream street canyons (Chew and Norford 2018; Ai and Mak 2017) is also valid for the building roofs with respect to time-averaged velocity profiles. However, this is not so evident for the streamwise turbulence intensity. (iii) Logarithmic law fitting ($R^2 = 0.99$), up to $Z/H \sim 2$ at $Re = 57000$ (Fig. 4) yielded a roughness length $z_0 \sim 1$ m in full scale, for a scale factor 1:150 ($H = 22.5$ m for the real building model) in the middle of the roof of the 4th building model ($Y/H = 0$, $X/H = -0.5$). According to VDI (2000), this corresponds to a very rough/urban upstream terrain. (iv) Preliminary examination of scale effects at $X/H = -0.5$, $Y/H = 0$, i.e. the centre of the roof of the 4th building (Fig. 4) shows no clear marks of Reynolds number dependence of the flow. Additional hot-wire measurements at $(X/H, Y/H, Z/H) = (-0.5, 0, 3)$ showed that the streamwise turbulence intensity varied from 12.5% to 13.5% between the examined Re number cases, which indicates that the Re-independent behaviour observed in Fig. 4 continues to be manifested even towards the free-stream region. The observed velocity differences at $(-0.5, 0, 3)$ between the examined Re numbers are also negligible (i.e. up to 2% of U_{ref}).

3.2 Flow structure inside the canyon

A three-dimensional representation of the flow structure at $Re = 23000$ and $Re = 57000$ is presented in Fig. 5 by means of stream traces, coloured with the non-dimensional vertical velocity values. The focus of this figure is on the region inside the canyon.

The shape and direction of the stream traces, as well as the positive and negative values of the vertical velocity close to the windward ($X \approx 0$) and leeward ($X \approx H$) walls of the canyon, respectively, are consistent with the existence of a canyon vortex. For both Reynolds numbers, the flow appears to be qualitatively symmetric with respect to the centre plane of the canyon ($Y = 0$).

Preliminary conclusions regarding scale effects can also be extracted, particularly for the region $Y > 0$ and $X \approx 0$, with higher W/U_{ref} values observed for $Re = 57000$ than for $Re = 23000$. A more thorough and quantitative analysis of Reynolds number independence will be given in the following sections.

3.3 Uncertainty quantification

A preliminary quantification of the underlying uncertainty of PTV measurements is presented here. The global uncertainty metric $\langle \epsilon_{pb,97.5\%} \rangle / U_{ref}$ (%), previously introduced in Sect. 2.4, is initially shown in Fig. 6a. It is reminded that this uncertainty metric quantifies the uncertainty of the particle tracks (prior to binning) and not that of the time-averaged results. For the time-averaged results, the uncertainty scales down with $\sqrt{N_t}$, with N_t being the number of vortex turnovers which is considered equal to the number of independent samples. It is seen that $\langle \epsilon_{pb,97.5\%} \rangle / U_{\mathrm{ref}}$ (%) is less than 4% for all three velocity components. In Fig. 6b, standard uncertainty ϵ_Q profiles (Eq. 6) at the centre line of the plane of symmetry ($Y/H = 0$), for U/U_{ref} and W/U_{ref} are given. The latter profiles are shown for both $Re = 23000$ and $Re = 57000$ and pertain to the time/ensemble-averaged results (i.e. after binning). The standard uncertainty is less than 3% at $X/H = 0.5$ which means that the low uncertainty values are maintained after binning (averaging).

Regarding the uncertainty linked to the calculation of the Reynolds number, Eqs. (17), (18) and (13) are implemented for all examined Reynolds numbers, i.e. for the different reference velocities. The necessary input is ϵ_p (see Eq. 13 and Appendix), $\epsilon_T = 1.3$ K, and $T = 307$ K. For the calculation of Re and its uncertainty, an overall average temperature—derived from all experimental runs with each corresponding to specific Re number—was utilised, instead of using the individual values pertaining to each case. For that reason, the uncertainty ϵ_T of the temperature was set equal to the standard deviation of the previous set of measurements (corresponding to individual Re numbers) instead of the accuracy of the measuring instrument (Sect. 2.3). If the accuracy of the measuring instrument was used instead, the uncertainty of Re would be underestimated. Finally, the Re number uncertainty ϵ_{Re} (Eq. 13) is at most ∼3.5% throughout the range $Re \in [23000, 57000]$, as already mentioned in Sect. 2.4.

3.4 Reynolds number sensitivity

Even at the initial stage of the analysis, it is clear that although the tested Reynolds numbers are above the critical values ($Re \sim 12000 - 17000$) found/adopted in the literature (Chew et al. 2018; Dsouza et al. 2024; VDI 2000; Snyder 1981; American Society of Civil Engineers 2012) for this type of applications, scale effects in specific regions of the whole measurement volume can be identified (Sect. 3.2). The present volumetric measurement method and uncertainty metrics provide the capacity for simultaneous pointwise and canyon-scale assessment. Pointwise (e.g. CTA) or planarwise (e.g. planar PIV) measurements are limited in this respect, especially when 3D flow phenomena are implicated.

3.4.1 Investigation in the plane of symmetry ($Y/H = 0$)

In order to examine scale effects on the centre plane of the canyon, contours of the time-averaged streamwise velocity are given in Fig. 7a and b for $Re = 23000$ (minimum) and $Re = 57000$ (maximum), respectively, along with (in plane) velocity vectors. By qualitatively comparing the results within the canyon corresponding to the minimum and maximum Reynolds numbers, the only noticeable difference is the magnitude of the negative streamwise velocity inside the street canyon which appears higher for $Re = 57000$ than for $Re = 23000$. The general flow structure, i.e. the number of formed vortices does not change with increasing Reynolds number as also concluded by Zhu and Chew (2025), for the case of $H/W = 1$. Furthermore, the position of the vortex core seems qualitatively stable between $Re = 23000$ and $Re = 57000$.

A more quantitative comparison follows in Fig. 7c and d, where the net difference (Eq. 9) is shown for the streamwise and the vertical velocity components, respectively. Figure 8 presents a similar analysis for the turbulence kinetic energy.

By observing the contours corresponding to the net difference, three different areas of interest for the three different variables have been traced (dashed line boxes): (i) $X/H \approx 0.6$ and $Z/H < 0.3$ for the streamwise velocity (Fig. 7c, region A), (ii) windward wall ($X/H \approx 1$) for the vertical velocity (Fig. 7d, region B), and (iii) leeward wall ($X/H \approx 0$)

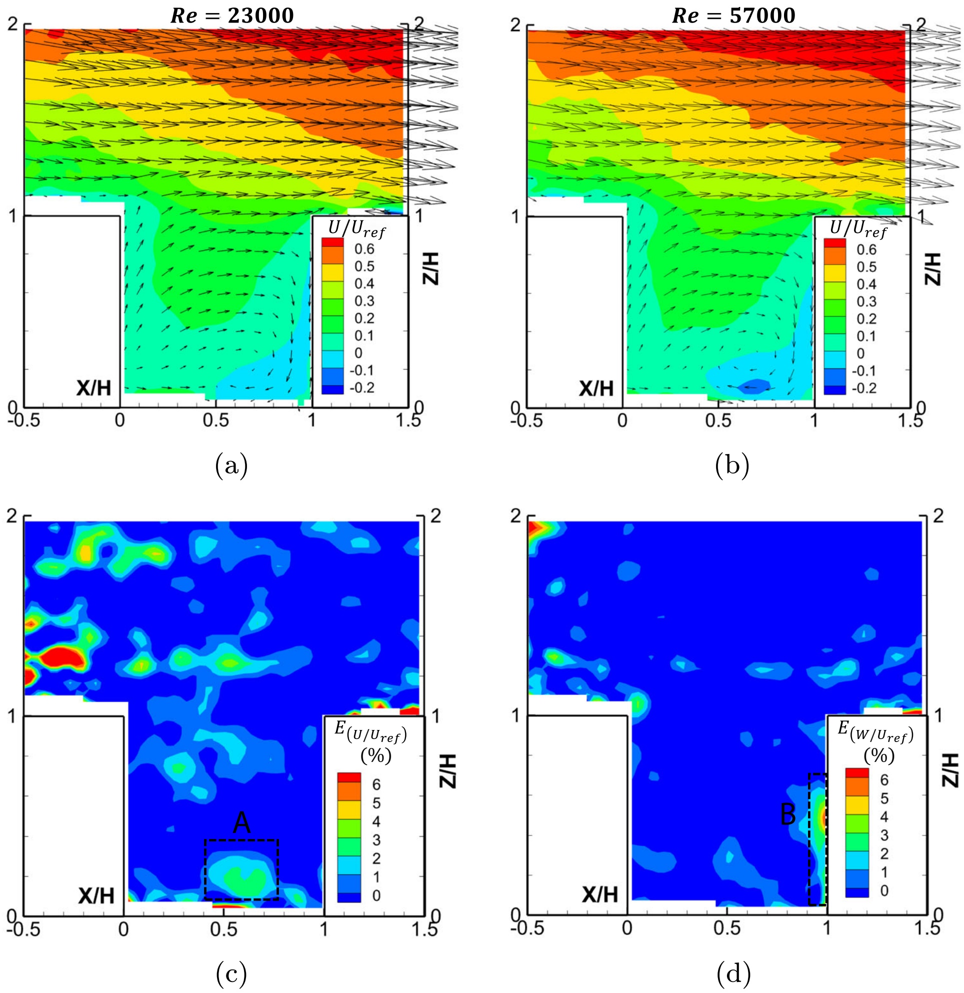

Fig. 7 Velocity vectors (tangent) and contours of the normalised mean streamwise velocity component U/U_{ref} for: **(a)** $Re = 23000$ and **(b)** $Re = 57000$, in the centre plane ($Y/H = 0$). Only some of the vectors (13% of their total number) are shown for the sake of clarity. **(c)** Net difference $E_{(U/U_{ref})} = \left|\Delta\left(U/U_{ref}\right)\right| - \epsilon_{|\Delta(U/U_{ref})|}$ (%) between $Re = 23000$ and $Re = 57000$ and (d) net difference $E_{(W/U_{ref})} = \left|\Delta\left(W/U_{ref}\right)\right| - \epsilon_{|\Delta(W/U_{ref})|}$ (%) between $Re = 23000$ and $Re = 57000$, again, at $Y/H = 0$. The flow is from left to right and U_{ref} is the free-stream velocity

for the turbulence kinetic energy (Fig. 8c, region C). These are areas of relatively high net difference (E_Q) values which is an indication of potentially significant scale effects. It is important to note that although Eqs. (6) and (8) link the standard uncertainty of the velocity and turbulence kinetic energy, respectively, to velocity standard deviation (which in turn is linked to turbulence intensity), there is not necessarily a strong correlation of the net difference E_Q (Eq. 9) with the local values of the turbulence intensity. This is clearly seen in Fig. 8c where the highest values of E_Q are encountered near the leeward wall (region C) although k does not demonstrate higher values there than in other regions inside the canyon. A similar statement can also be made for regions A and B (Fig. 7c and d, respectively), corresponding to the streamwise and the vertical velocity, when juxtaposed with Fig. 8a, b. Since the standard uncertainty for $Q = U/U_{ref}, V/U_{ref}$ or $W/U_{ref}, \epsilon_{\Delta Q}$ (Eq. 5), is a function of σ_Q (Eq. 6), expressing the level of turbulence in the flow, a more definite way to test the correlation between the net difference E_Q and the local turbulence levels is to calculate the R^2 value between E_Q and $\epsilon_{\Delta Q}$. A similar reasoning also applies to k/U_{ref}^2 with the only difference being that $\epsilon_{\Delta Q} = f(\sqrt{\sigma_U^4 + \sigma_V^4 + \sigma_W^4})$ (Eq. 8). Finally, by adjusting and implementing Eq. (10) ($x = E_Q$ and $y = \epsilon_{\Delta Q}$) for the region inside and around the canyon (i.e. $Z/H < 1$), it is concluded that R^2 is less than 0.14 for all velocity components and 0.37 for k/U_{ref}^2. These values are indicative of low correlation between E_Q and $\epsilon_{\Delta Q}$. Therefore, E_Q does not seem to significantly favour regions of lower turbulence intensity by deeming them Re-insensitive.

Finally, line plots are provided pertaining to the aforementioned areas of interest, for U/U_{ref} (Fig. 9a), W/U_{ref} (Fig. 9c) and k/U_{ref}^2 (Fig. 9d), respectively. Error bars for both the velocity and the turbulence kinetic energy profiles, corresponding to the standard uncertainty calculated by implementing Eqs. (6) and (8), are also included for $Re = 23000$. Although, in certain occasions, the differences between $Re = 23000$ and $Re \neq 23000$ are marginally larger than the error bars for the streamwise velocity at $Y/H = 0$, $X/H = 0.6$ (Fig. 9a), no clear trend of scale effects can be discerned. This is not the case for the vertical velocity

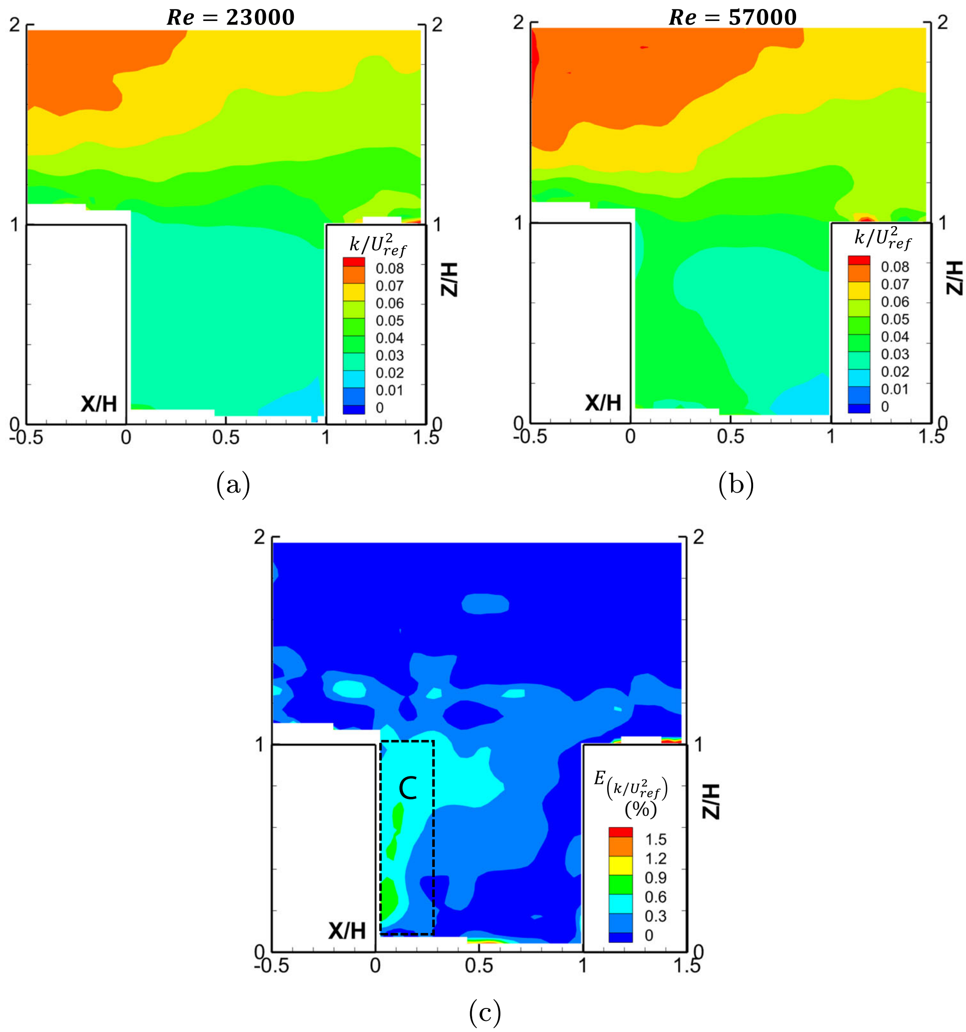

Fig. 8 Contours of the normalised turbulence kinetic energy k/U^2_{ref} for: **(a)** Re = 23000 and **(b)** $Re = 57000$, in the centre plane ($Y/H = 0$). **(c)** Net difference $E_{(k/U^2_{ref})} = \left|\Delta\left(k/U^2_{ref}\right)\right| - \epsilon_{\left|\Delta\left(k/U^2_{ref}\right)\right|}$ (%) between $Re = 23000$ and $Re = 57000$, at $Y/H = 0$. The flow is from left to right and U_{ref} is the free-stream velocity

(Fig. 9c) at $Y/H = 0$ and $X/H = 0.99$ (windward wall) since there is an almost monotonically increasing trend of the velocity values with increasing values of the Reynolds number for $Z/H < 1$ and especially around $Z/H = 0.5$. The maximum net difference values for the vertical velocity are also encountered around $Z/H = 0.5$ (Fig. 7d). Additionally, the differences between $Re = 47000$ and $Re = 23000 - 37000$, around $Z/H = 0.5$, are clearly larger than the error bars. For the turbulence kinetic energy (Fig. 9d) near the leeward wall ($Y/H = 0$ and $X/H = 0.02$) and for $Z/H < 1$ (i.e. within the canyon), a clear converging trend with increasing Re number is observed. A comparison of the line plots shown in Fig. 9c and d, indicating the existence of scale effects, with the ones shown in Fig. 9b (leeward wall, W/U_{ref}) and Fig. 9e (windward wall, k/U^2_{ref}), respectively, where E_Q demonstrates relatively low values, clearly verifies the previous findings. In particular, no clear trend with increasing Re number is observed for W/U_{ref} at the leeward wall and k/U^2_{ref} at the windward wall. In conclusion, there is generally a consistency between the regions identified by the net difference indicator as the ones which are the most susceptible to scale effects and the regions identified by means of line plot comparisons.

3.4.2 Canyon-scale investigation

In this section, a canyon-scale investigation (i.e. in the whole measurement volume) is undertaken with focus on the data inside and around ($Z/H < 1$) the canyon. Firstly, $Q = U/U_{ref}, V/U_{ref}, W/U_{ref}$, and k/U^2_{ref} results at $Re = 57000$ are plotted against the respective ones at $Re = 23000$ in Fig. 10. Indices 57 and 23 correspond to $Re = 57000$ and $Re = 23000$, respectively. If Reynolds number independence is accomplished, then the results should follow the line $y = x$. Point clusters in red and blue correspond to the top 1% of the data with maximum net difference (Eq. 9) values, i.e. $E_Q \geq 0.99[E_Q]_{max}$. Red points correspond to the positive values of U/U_{ref}, V/U_{ref} or W/U_{ref} at $Re = 57000$, while blue points represent negative values (again at $Re = 57000$),

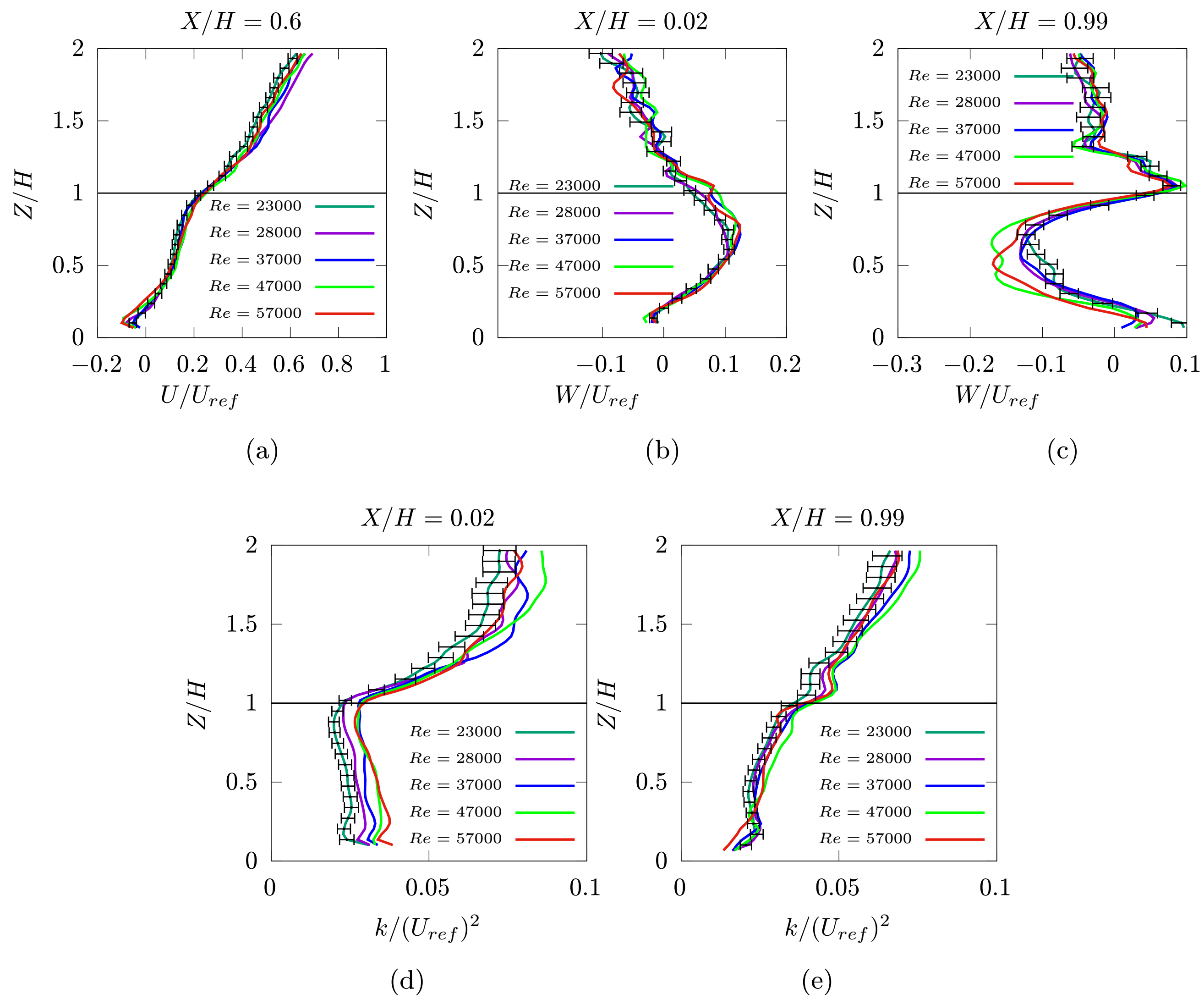

Fig. 9 Profiles of the non-dimensional: **(a)** mean streamwise velocity (U/U_{ref}) at $Y/H = 0$ and $X/H = 0.6$, **(b)** and **(c)** mean vertical velocity (W/U_{ref}) at $X/H = 0.02$ (leeward wall) and $X/H = 0.99$ (windward wall), respectively, **(d)** and **(e)** turbulence kinetic energy (k/U_{ref}^2) at $X/H = 0.02$ (leeward wall) and $X/H = 0.99$ (windward wall), for $Re \in [23000, 57000]$. U_{ref} is the free-stream velocity. All results pertain to the plane of symmetry ($Y/H = 0$)

in Fig. 10a–c, respectively. The data points with values within 1% of the maximum net difference for k/U_{ref}^2 are represented by black points in Fig. 10d. Green points correspond to the other 99% of the points ($E_Q < 0.99[E_Q]_{max}$). This colour coding facilitates the extraction of qualitative conclusions regarding coherent spatial regions susceptible to scale effects and will also be used to implicitly and quantitatively represent these effects in the following scatter plots.

By examining Fig. 10, the following general conclusions are extracted: (i) the net difference indicator is capable of consistently identifying deviating patterns from the $y = x$ line within the examined dataset. Since the net difference indicator is free of any (standard) measurement uncertainty, these patterns are linked to scale effects as will be shown below. (ii) For the velocities (shown in Fig. 10a–c), positive values (red points) corresponding to the top 1% are almost always in the $y < x$ region. The opposite applies to the negative velocities. For the vertical velocity (W), the underestimation of its magnitude at $Re = 23000$ is clearly translated to an underestimation of the strength of the vortical structure inside the canyon as will be shown in the rest of this section and was preliminarily discussed in Sect. 3.2. The same conclusion applies also to the underestimation of the magnitude of negative values (blue points) of the streamwise velocity, shown in Fig. 10a. (iii) For U/U_{ref} and k/U_{ref}^2, the top 1% of the data with maximum net difference significantly and visibly deviate from the $y = x$ line and from the other 99% of

Fig. 10 **(a)** Normalised streamwise velocity U/U_{ref}, **(b)** normalised lateral velocity V/U_{ref}, **(c)** normalised vertical velocity W/U_{ref} and **(d)** normalised turbulence kinetic energy k/U^2_{ref} at $Re = 57000$ plotted against the respective results at $Re = 23000$. Indices 23 and 57 correspond to $Re = 23000$ and 57000, respectively. The line $y = x$ is also plotted for every variable. In sub-figures a-c, point clusters in red and blue correspond to the top 1% of the data with maximum net difference (Eq. 9) values, i.e $E_Q \geq 0.99[E_Q]_{max}$. Red corresponds to positive velocity values at $Re = 57000$ while blue to negative ones. The top 1% is represented by black points in (d). All figures pertain to the region inside and around the street canyon ($Z/H < 1$)

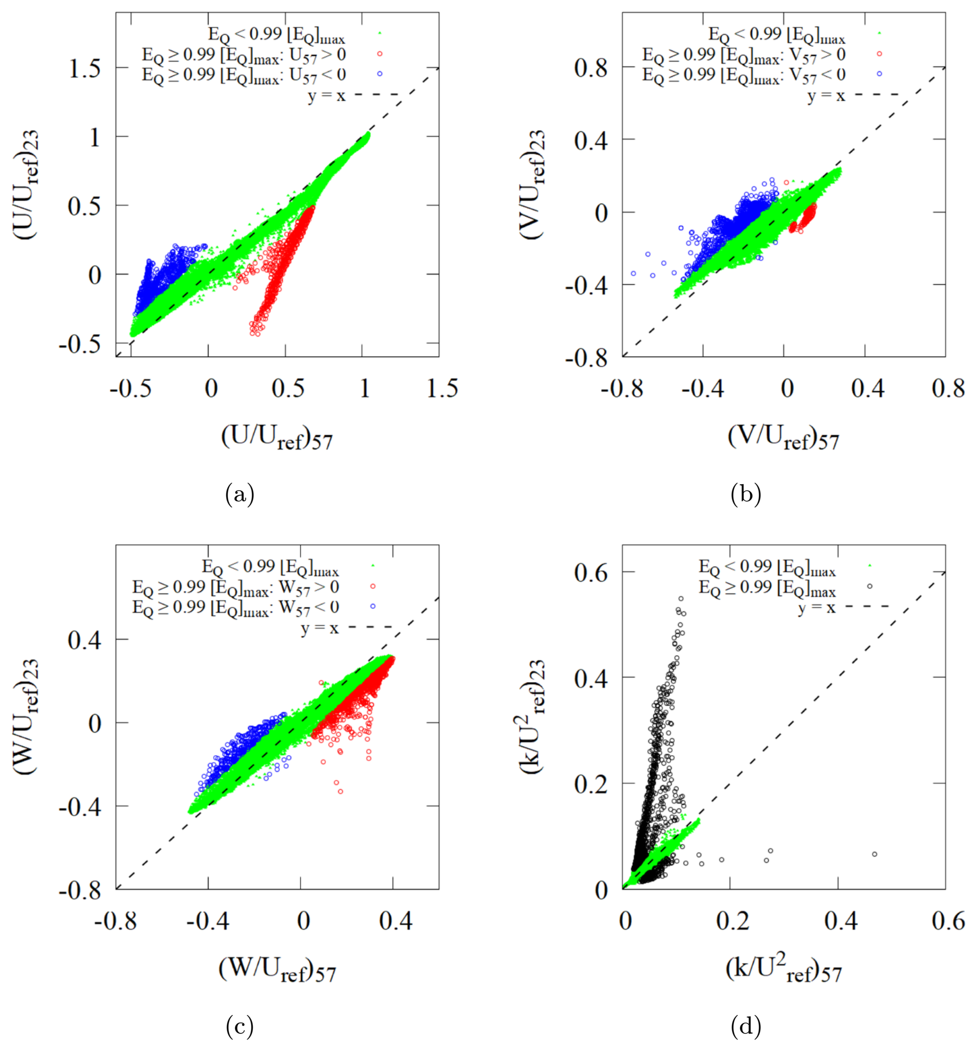

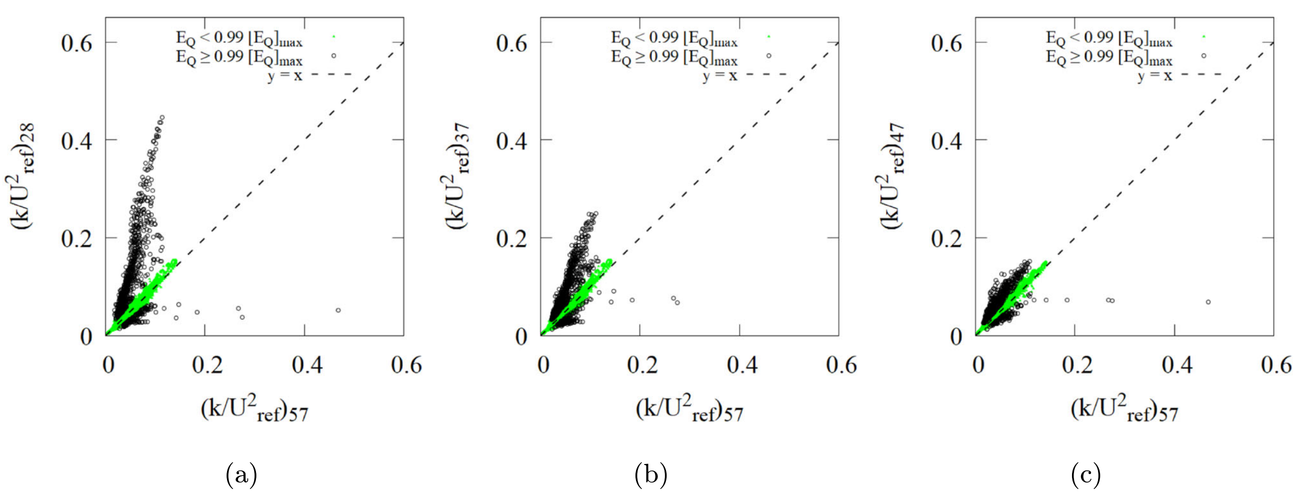

Fig. 11 Normalised turbulence kinetic energy k/U^2_{ref} at $Re = 57000$ plotted against the respective results at: **(a)** $Re = 28000$ (index 28), **(b)** $Re = 37000$ (index 37) and ((**c**)) $Re = 47000$ (index 47). Point clusters in black and green correspond to the top 1% ($E_Q \geq 0.99[E_Q]_{max}$) and the bottom 99% ($E_Q < 0.99[E_Q]_{max}$) of the data with maximum net difference values (Eq. 9), respectively. All figures pertain to the region inside and around the street canyon ($Z/H < 1$)

the points. Comparisons, in the form of scatter plots between $Re = 57000$ and $23000 < Re < 57000$, indicate the disappearance of these deviating patterns above $Re = 37000$ and $Re = 47000$ for U/U_{ref} and k/U_{ref}^2, respectively. This comparison is shown here only for k/U_{ref}^2 in Fig. 11.

The regions incorporating the points within 1% of the maximum net difference can be plotted in space separately for every variable, for the sake of clarity. Firstly, the coordinates of the red and blue points of the streamwise velocity (Fig. 10a) are plotted in Fig. 12.

By examining the topology of the points corresponding to the top 1% of maximum net difference, one can observe that negative and positive U/U_{ref} values are roughly separated into two different regions, i.e. outside and inside the canyon, respectively, while they are both encountered close to the ground. The region of positive velocities corresponds to the laterally developed boundary layer, outside the canyon. The negative velocities inside the canyon and near the ground are linked to the existence of the canyon vortex, since due to the latter flow feature the streamwise velocity is always negative there. To quantify the critical Reynolds number of the flow, contours of the net difference are given for the streamwise velocity at $Y/H = 2.5$ (Fig. 13), since this plane intersects with one of the two main regions identified by the previous analysis. Results for the region outside the canyon are not shown here, since similar conclusions are derived with respect to the critical Re number. It is reminded that the latter regions are expected to be the most susceptible to Re-dependence, since they correspond to the points that deviate the most from $y = x$ in Fig. 10. Results are given not only for $Re = 23000$ and $Re = 57000$ (Fig. 13a) but also for the net difference between $Re = 37000$ and $Re = 57000$ (Fig. 13b). Velocity vectors of U, W (tangent) at $Re = 57000$ are also included to give an idea of the flow structure in the examined plane. It is observed that at $Y/H = 2.5$ there are relatively high values of net difference between $Re = 23000$ and $Re = 57000$, indicating the susceptibility of these regions to scale effects. However, this is not the case for the difference between $Re = 37000$ and $Re = 57000$, which is significantly reduced in comparison with that between $Re = 23000$ and $Re = 57000$. The extent of the high net difference regions as well as the values of the latter metric is still relatively large when this difference is calculated between $Re = 28000$ and $Re = 57000$ (not shown here). The final conclusion from this analysis is that a value of at least $Re = 37000$ is necessary to ensure canyon-scale Re-independence for the streamwise velocity.

Similar representation as in Fig. 12 is given in Fig. 14 for the vertical velocity W/U_{ref}. The main observation is that negative and positive velocities (at $Re = 57000$) belonging to the data within 1% of the maximum net difference are clearly separated into two different regions, i.e. near the windward and the leeward walls of the examined canyon. These points are part of the vortex formed in this region, indicating that at the minimum Re number the vortical structure is relatively less strong.

As for the streamwise velocity, contours of the net difference are given for the vertical velocity at $Y/H = 2.5$, for $Re = 23000, 57000$ and $Re = 37000, 57000$, in Fig. 15. It is observed that the extended regions of high (i.e $> 6\%$) net difference between $Re = 23000$ and $Re = 57000$ almost disappear when this metric is calculated for $Re = 37000, 57000$. There are still some limited regions of high net difference close to the walls though. In conclusion, there seem to be Reynolds number effects persisting even up to $Re = 37000$ for the vertical velocity, which may appear even at higher values as one approaches the walls.

A similar analysis is then conducted for the lateral velocity, V/U_{ref}, and shown in Figs. 16 and 17. As in the case of the streamwise velocity, Fig. 16 shows that the top 1% data are roughly separated into two regions, i.e. outside ($V_{57} > 0$) and inside the canyon ($V_{57} < 0$). The region inside the canyon is mainly of interest here for two reasons: firstly, the points outside are significantly less than the points inside the canyon (i.e. $\sim$10% of the latter), and secondly, the region inside the canyon partially overlaps with the respective identified regions for both U/U_{ref} and W/U_{ref}. At the same time, this area contains part of the vortical structure formed inside the canyon. Despite of the above-mentioned overlap, it should be clarified that strong "uncorrelation" (or correlation) between two different Re numbers for one velocity component in a specific region does not always translate to strong "uncorrelation" (or correlation) for the other velocity components in the same region. This may be attributed to the fact that the velocity components themselves are not always strongly correlated with each other. For example, when the magnitude of W is maximum inside the street canyon (leeward and windward wall), U is close to zero and vice versa, due to the presence of the canyon vortex.

Figure 17 shows that the existing high net difference regions between $Re = 23000$ and 57000 almost vanish for $Re = 37000$. It is important to note that this is in not the case for the net difference between $Re = 28000$ and 57000 (not shown here), where these high $E_{(V/U_{ref})}$ regions are still clearly discernible with values reaching 15%. Therefore, it can be safely stated that $Re > 37000$ ensures Re-independence for the lateral velocity in the examined framework.

Finally, the same analysis is undertaken for the turbulence kinetic energy and the coordinates of the points corresponding to the top 1% of the data (see Fig. 10d) are given in Fig. 18. In this figure, it is observed that the points span regions inside and outside the canyon. Here, net difference contours are given only at $Y/H = 4.31$ (outside the canyon) in Fig. 19. The points in this area roughly constitute the top $0.3-0.4\%$

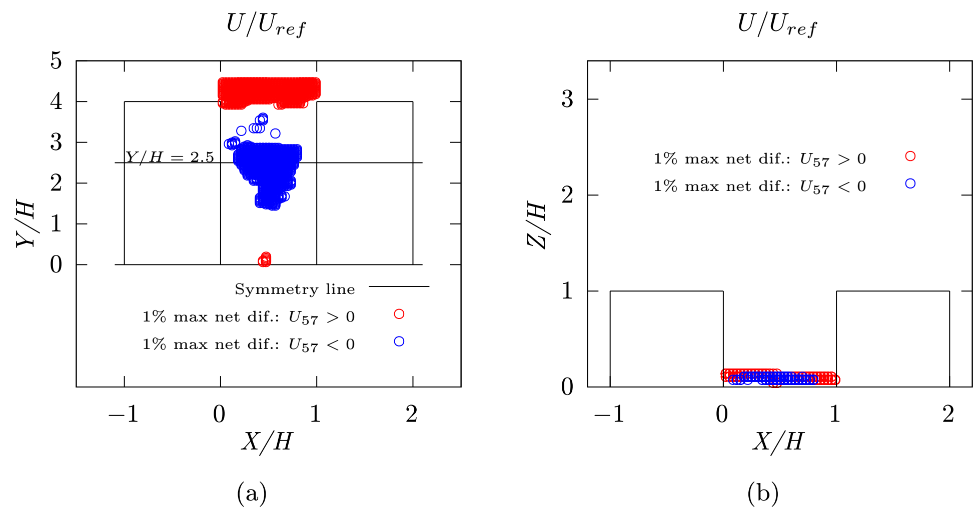

Fig. 12 **(a)** Y/H, X/H (top view) and **(b)** Z/H, X/H (side view) coordinates of the points corresponding to the 1% of the data inside and around ($Z/H < 1$) the canyon with maximum values of net difference $E_{(U/U_{ref})} = \left|\Delta\left(U/U_{ref}\right)\right| - \epsilon_{|\Delta(U/U_{ref})|}$. Red points correspond to positive velocity values at $Re = 57000$ while blue to negative ones. The flow is from left to right

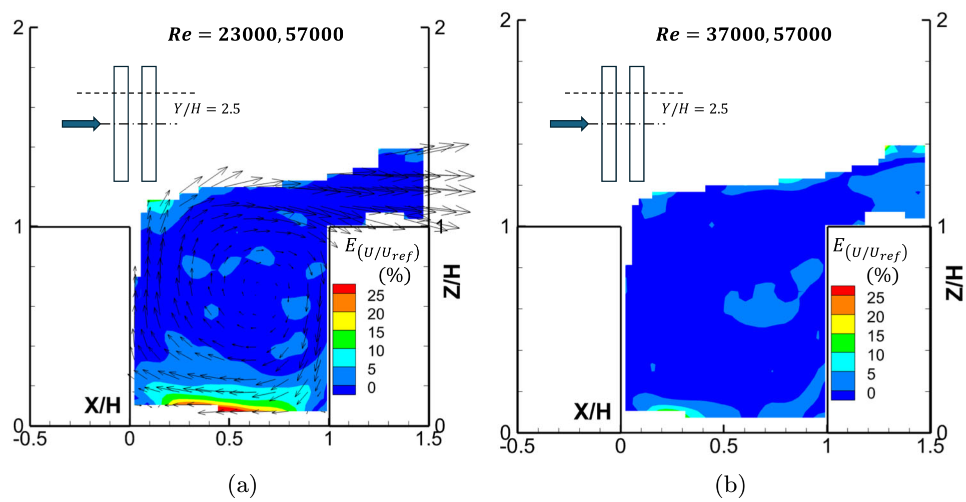

Fig. 13 **(a)** Net difference $E_{(U/U_{ref})} = \left|\Delta\left(U/U_{ref}\right)\right| - \epsilon_{|\Delta(U/U_{ref})|}$ (%) between $Re = 23000$ and $Re = 57000$, at $Y/H = 2.5$ (see Fig. 12). Velocity vectors of U, W (tangent) at $Re = 57000$ are also included but only some of them ($\sim 20\%$) for the sake of clarity. **(b)** The same as in (a) but between $Re = 37000$ and $Re = 57000$

of the data with maximum net difference. Figure 19 shows that the net difference is largely reduced to less than 1% when calculated between $Re = 47000$ and 57000 for the examined plane.

As a final step, the squared correlation coefficient R^2 (Eq. 10) and the normalised mean square error MSE^* (Eq. 12) are applied as means of global investigation of scale effects. The closer the R^2 value is to 1, the stronger is the correlation between the examined variables. On the other hand, values of the MSE^* close to zero indicate relatively small scattering around the $y = x$ line. The respective results are shown in Fig. 20a and b. By making use of this information, R^2 and MSE^* can be combined in the following new metric: $SCM = \sqrt{(R^2 - 1)^2 + (MSE^*)^2}$ with SCM standing for *scattering correlation metric*. For “perfect” agreement between the examined variables, the value of the later metric should be zero. The metric SCM is shown in Fig. 20c.

As a minimum requirement for Reynolds number independence, SCM, R^2, and MSE^* should stabilise and plateau beyond a critical Reynolds number. All employed canyon-scale metrics imply that the streamwise velocity is relatively insensitive to Reynolds number as soon as $Re \geq 23000$. For the vertical (W/U_{ref}) and the lateral velocity (V/U_{ref}), this happens for $Re \geq 37000$ while for k/U_{ref}^2 the convergence of the global (canyon-scale) metrics to an asymptotic value is not so apparent, indicating that even at $Re = 47000$, Reynolds number independence is not categorically ensured.

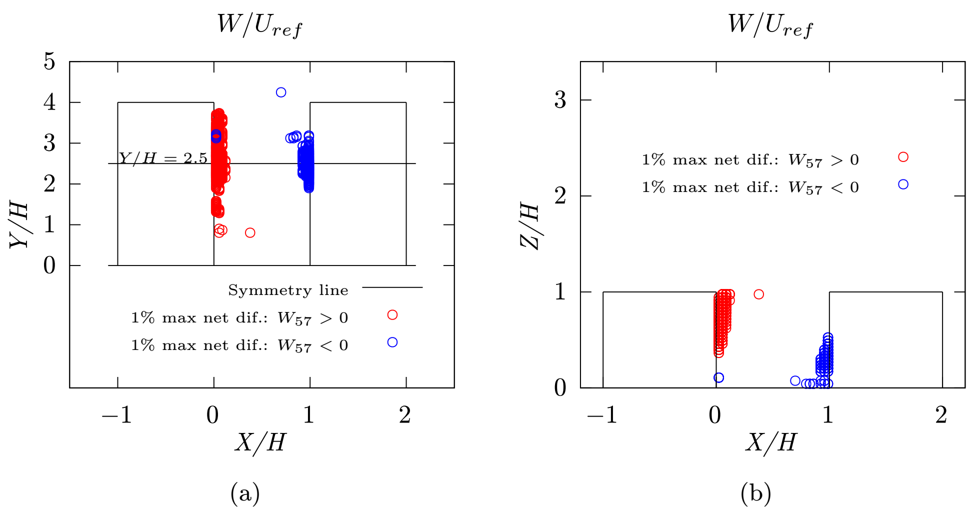

Fig. 14 **(a)** Y/H, X/H (top view) and **(b)** Z/H, X/H (side view) coordinates of the points corresponding to the 1% of the data inside and around ($Z/H < 1$) the canyon with maximum values of net difference $E_{(W/U_{ref})} = \left|\Delta\left(W/U_{ref}\right)\right| - \epsilon_{|\Delta(W/U_{ref})|}$. Red points correspond to positive velocity values at $Re = 57000$ while blue to negative ones. The flow is from left to right

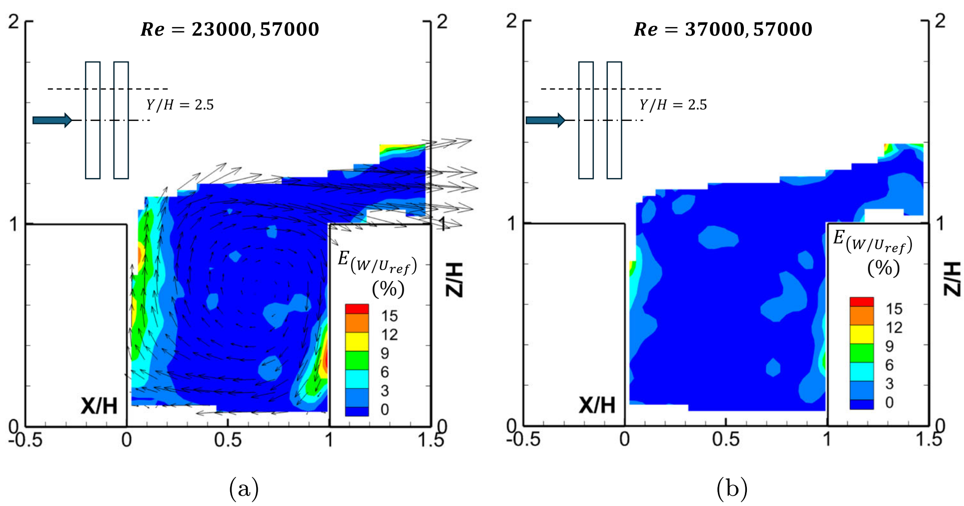

Fig. 15 **(a)** Net difference $E_{(W/U_{ref})} = \left|\Delta\left(W/U_{ref}\right)\right| - \epsilon_{|\Delta(W/U_{ref})|}$ (%) between $Re = 23000$ and $Re = 57000$, at $Y/H = 2.5$ (see Fig. 14). Velocity vectors of U, W (tangent) at $Re = 57000$ are also included but only some of them ($\sim 20\%$) for the sake of clarity. **(b)** The same as in (a) but between $Re = 37000$ and $Re = 57000$

The metrics SCM, R^2, and MSE^* have been calculated with $Re = 57000$ being always the reference. Hence, for the sake of completeness, a new global metric which is calculated between subsequent Re numbers is introduced and given in the following equation:

$$r_{L_2}(E_Q, \Delta Re) = \frac{\left\|E_Q\right\|_2}{\left\|(Q_{Re_{i+1}} + Q_{Re_i})/2\right\|_2} \cdot \frac{\Delta Re_{\max}}{Re_{i+1} - Re_i} \tag{15}$$

where $\left\|E_Q\right\|_2$ is the L_2 norm of the net difference (assessed only for $E_Q > 0$), $\left\|(Q_{Re_{i+1}} + Q_{Re_i})/2\right\|_2$ is the L_2 norm of the examined variable ($Q = U/U_{ref}$, V/U_{ref}, W/U_{ref}, k/U_{ref}^2), $\Delta Re_{\max}$ is the maximum range between subsequent Re numbers (equal to 10000), and $i = 1, 2, 3, 4$ or 5 corresponds to the five examined Re numbers. The L_2 ratio is multiplied by the second term, which accounts for the Re number range, in order to adjust for differences in the increments between successive Re values. Note that all the L_2 norms are evaluated by summing over the entire measurement volume. The introduced metric is plotted against $Re_{i+1/2} = (Re_{i+1} + Re_i)/2$ in Fig. 20d.

Figure 20d shows that the metric $r_{L_2}(E_Q, \Delta Re)$ decreases from the first to the second ΔRe step while it remains

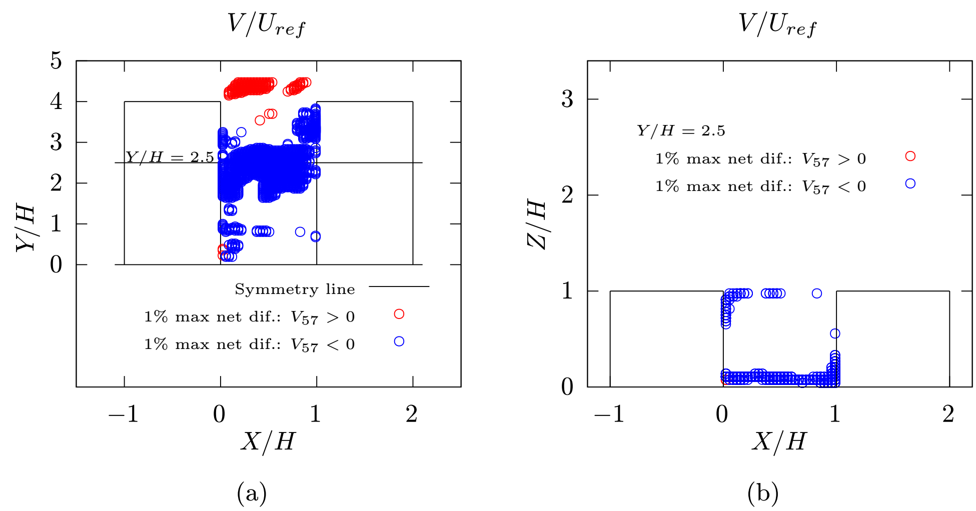

Fig. 16 **(a)** Y/H, X/H (top view) and **(b)** Z/H, X/H (side view) coordinates of the points corresponding to the 1% of the data inside and around ($Z/H < 1$) the canyon with maximum values of net difference $E_{(V/U_{ref})} = \left|\Delta\left(V/U_{ref}\right)\right| - \epsilon_{|\Delta(V/U_{ref})|}$. Red points correspond to positive velocity values at $Re = 57000$ while blue to negative ones. The flow is from left to right

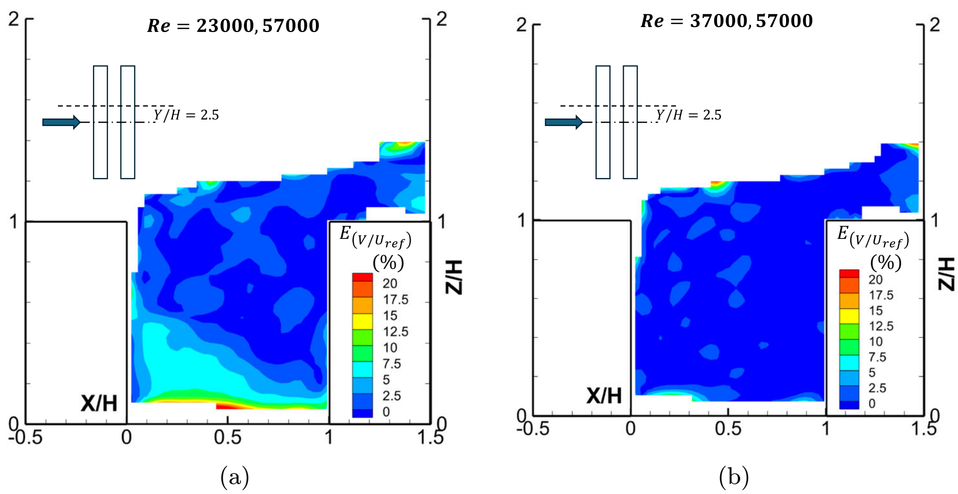

Fig. 17 **(a)** Net difference $E_{(V/U_{ref})} = \left|\Delta\left(V/U_{ref}\right)\right| - \epsilon_{|\Delta(V/U_{ref})|}$ (%) between $Re = 23000$ and $Re = 57000$, at $Y/H = 2.5$ (see Fig. 16). **(b)** The same as in (a) but between $Re = 37000$ and $Re = 57000$

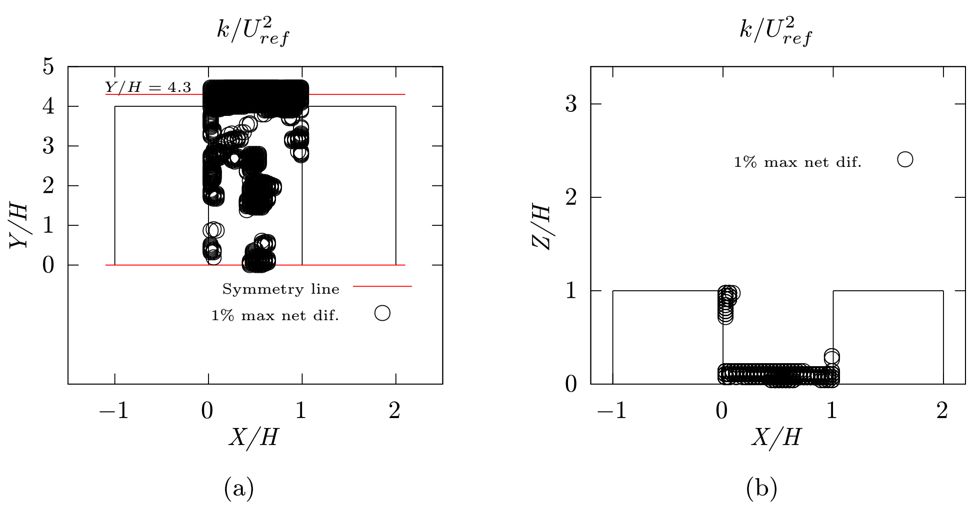

Fig. 18 **(a)** Y/H, X/H (top view) and **(b)** Z/H, X/H (side view) coordinates of the points corresponding to the 1% of the data inside and around ($Z/H < 1$) the canyon with maximum values of net difference $E_{(k/U^2_{ref})} = \left|\Delta\left(k/U^2_{ref}\right)\right| - \epsilon_{\left|\Delta\left(k/U^2_{ref}\right)\right|}$. The flow is from left to right

relatively stable after that, for all the examined variables. In general, this is an indication that in terms of net difference, Re-independence is widely achieved in the range $Re \in (37000, 47000)$. However, it should be noted that,

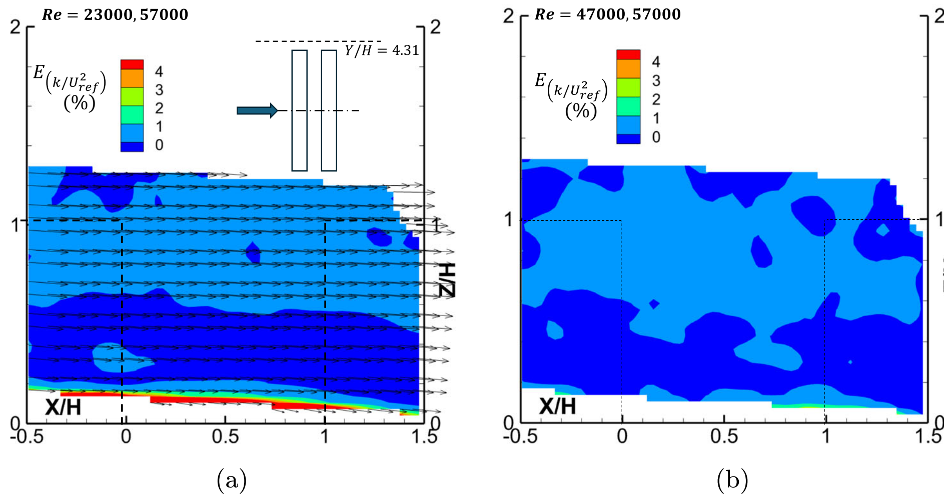

Fig. 19 **(a)** Net difference $E_{(k/U_{ref}^2)} = \left|\Delta\left(k/U_{ref}^2\right)\right| - \epsilon_{\left|\Delta\left(k/U_{ref}^2\right)\right|}$ (%) between $Re = 23000$ and $Re = 57000$, at $Y/H = 4.3$ (see Fig. 18). Velocity vectors of U, W (tangent) at $Re = 57000$ are also included but only some of them ($\sim 20\%$) for the sake of clarity. **(b)** The same as in (a) but between $Re = 47000$ and $Re = 57000$

unlike U/U_{ref}, there are some oscillations around an asymptotic value for all the other variables which could be an indication of incomplete convergence with respect to the Re number.

4 Conclusions

Scale effects on an urban street canyon configuration have been experimentally investigated with canyon-scale 3D-3C PTV measurements. The configuration consisted of 5 subsequent and identical street canyons with aspect ratios $H/W = 1$ and $L/H = 8$. The present attempt included both 3D-3C Robotic Particle Tracking Velocimetry and Constant Temperature Anemometry measurements and focused on time-averaged velocity as well as turbulence kinetic energy data. An important part of the current attempt is the creation of a framework which takes into account the spatial distribution of the underlying standard uncertainty, thereby facilitating the local separation of actual Reynolds number dependence from measurement uncertainty. The results were complemented by global indices applied to the whole measurement volume such as the squared correlation coefficient, the (normalised) mean square error, and their combination through the scattering correlation metric (SCM).

The main conclusions regarding Reynolds number independence of the examined flow are the following:

- The main mean flow structure—namely, the existence and position of a single canyon vortex—remained unchanged in the examined Re range ($Re > 23000$). This is in agreement with the commonly stated critical Reynolds number of $Re > 10000 - 20000$.
- The local and global (canyon-scale) metrics applied here revealed that the critical Reynolds number can be as high as $Re = 47000$ if all variables are examined, i.e. the three velocity components and the turbulence kinetic energy, throughout the canyon. The critical Re value may be even higher for the vertical velocity in close proximity of the canyon walls.
- The regions of the canyon most susceptible to scale effects are mainly those concentrated close to wall boundaries and at around one quarter of the canyon length away from its lateral end, i.e. at $Y/H = 2 - 3$. For the streamwise and the lateral velocity components, the areas that are the most sensitive to the Re number are close to the bottom of the canyon. For the vertical velocity component, these areas are mainly encountered close to the windward and leeward walls of the canyon, where this component's magnitude is the highest. In general, scale effects are mainly manifested as a weaker vortical structure developing in the region around $Y/H = 2.5$.
- The analysis implemented here also revealed a region located outside of the canyon, i.e. at $Y/H = 4.31$ (the edge of the canyon is located at $Y/H = 4$) and close to the ground where all examined variables, except the vertical velocity (W/U_{ref}), demonstrated Re-dependent behaviour.
- The employment of global metrics such as the correlation coefficient R^2 and the normalised mean square error MSE^* indicated an increased Reynolds number sensitivity of V/U_{ref} and k/U_{ref}^2, compared with the other two variables.
- The utilisation of scatter plots between different Reynolds numbers in conjunction with the novel *net difference*

Fig. 20 **(a)** Squared correlation coefficient R^2, **(b)** normalised mean square error MSE^* and **(c)** combined metric $SCM = \sqrt{(R^2-1)^2 + (MSE^*)^2}$. The above-presented metrics are implemented for $Re = 23000$, 28000, 37000, 47000 with respect to $Re = 57000$ used as reference. **(d)** $r_{L_2}(E_Q, \Delta Re)$ metric which is based on the net difference between subsequent Re numbers. Results are shown for all examined variables and were extracted by making use of all available measurements

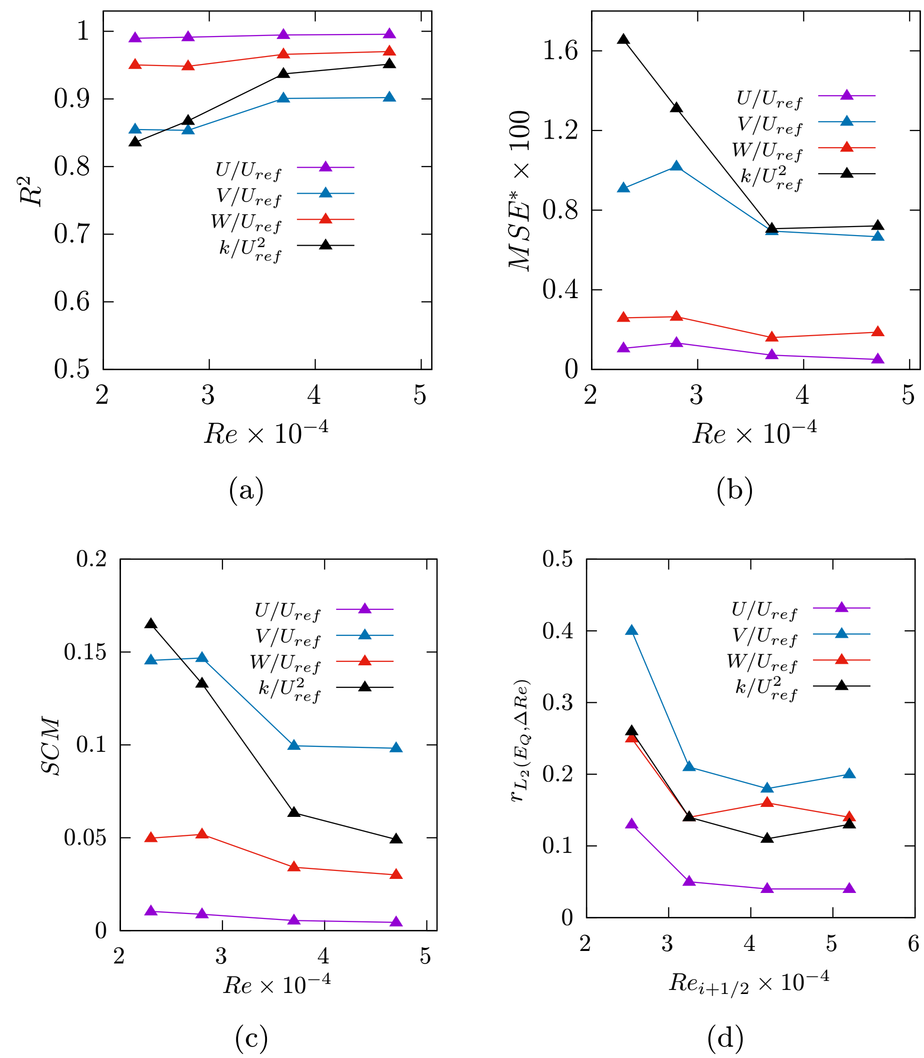

indicator is capable of reliable, efficient, and easy identification of regions which are the most susceptible to scale effects, within the whole measurement volume.

A general conclusion is that Re dependency of flow quantities in specific regions may persist above the widely adopted critical values of the Reynolds number (e.g. in the range 10000–20000, at least in cases similar to the one examined here). This is particularly evident in the proximity of wall boundaries. Net difference values around 10% of the reference velocity (U_{ref}), which were identified in various occasions in this study, correspond to at least 33% of the local velocity difference within the canyon ($U_c/U_{ref} \approx 0.3$, Eq. 1). This indicates that the scale effects observed throughout this work cannot be neglected as they are expected to have important implications in the discipline of urban flows. In pollutant dispersion studies in the urban environment, the source is commonly located near the ground level and openings to the buildings are at the canyon walls. It is therefore common to perform measurements in the proximity of these regions. Furthermore, in wind tunnel studies focusing on air ventilation, the flow structure (especially the velocity fluctuations) near the walls and openings of the examined building(s) is crucial. Another area of interest is when assessing wind load on buildings and structures (see Appendix).

The developed analytical and investigative tools presented here could be successfully applied to other cases where the investigation of scale effects is the primary target, as long as the uncertainty is carefully quantified at every step of the measurement procedure. An important future endeavour is to conduct a similar analysis for urban street canyon cases with different upstream conditions, e.g. an atmospheric boundary layer flow. Future attempts involving the obtained dataset could also span disparate research directions, such as the study of street canyon air ventilation, the deeper investigation of turbulence statistics focusing on their spanwise variation, or even data assimilation.

Appendix

In Appendix, more details regarding the uncertainty quantification analysis employed are included. Firstly, the Sutherland's formula (White 2006) for the calculation of the dynamic viscosity is given:

$$\mu(T) = \mu_0 \left(\frac{T}{T_0}\right)^{\frac{3}{2}} \frac{T_0 + C}{T + C} \tag{16}$$

with $\mu_0 = 1.716 \cdot 10^{-5}$ kg/(m·s), $T_0 = 273.15$ K, and $C = 111$ K denoting the reference dynamic viscosity, reference temperature, and Sutherland's constant, respectively. T is the absolute temperature at which the viscosity $\mu(T)$ is evaluated. Sutherland's formula is needed for the calculation of the Reynolds number as well as its uncertainty.

The density can be calculated through the equation of state of ideal gases. If the uncertainty of the barometric pressure is ignored, then the following equation holds for the uncertainties of the dynamic viscosity and the density, which was derived by means of uncertainty propagation:

$$\left(\epsilon_\mu^2, \epsilon_\rho^2\right) = \left[\left(\frac{d\mu}{dT}\right)^2 \cdot \epsilon_T^2, \left(\frac{d\rho}{dT}\right)^2 \cdot \epsilon_T^2\right] \tag{17}$$

where the (squared) uncertainty of the dynamic viscosity and of the density, ϵ_μ^2 and ϵ_ρ^2, is contained in a single vector for the sake of conciseness. It can be easily seen that the derivatives found in Eq. (17) are calculated by using Eq. (16) and the equation of state of the ideal gases, for the dynamic viscosity and the density, respectively.

The free-stream velocity U_{ref} is extracted by measuring the dynamic pressure (p) through a Pitot-static tube connected to a pressure transducer. Therefore, it is a function of the dynamic pressure and the density. Then, the following equation can be derived:

$$\epsilon_{U_{ref}} = \sqrt{\left(\frac{\partial U_{ref}}{\partial p}\right)^2 \cdot \epsilon_p^2 + \left(\frac{\partial U_{ref}}{\partial \rho}\right)^2 \cdot \epsilon_\rho^2} \tag{18}$$

where the density and the dynamic pressure are considered uncorrelated (incompressible flow).

All mathematical expressions of the derivatives implicated in the previous equations as well as those of Sect. 2.4 are provided in Table 1, where $P = 101325$ Pa (barometric pressure), $M = 0.029$ kg/mol (molar mass of air), $R = 8.31$ [J/(mol·K)] (universal gas constant). It is reminded that the density is calculated through the ideal gas law, i.e. $\rho = \dfrac{PM}{RT}$. All the other variables have been explained throughout the text. The third column of this table indicates the equation label associated with each derivative.

Table 1 Summary of derived mathematical expressions for the uncertainty quantification presented in Sect. 2.4, including their respective equation references

Derivative or variable	Mathematical expression	Equation reference
$\frac{\partial \rho}{\partial T}$	$-\frac{PM}{RT^2}$	(17)
$\frac{\partial U}{\partial \rho}$	$-\frac{1}{2}\sqrt{\frac{2p}{\rho^3}}$	(18)
$\frac{\partial U}{\partial p}$	$\frac{1}{2}\sqrt{\frac{2}{\rho \cdot p}}$	(18)
$\frac{\partial \mu}{\partial T}$	$\frac{\mu_0 \sqrt{T}(T_0 + C)}{T_0^{3/2}} \frac{T + 3C}{2(T + C)^2}$	(17)
$\frac{\partial Re}{\partial \rho}$	$\frac{U_{ref} H}{\mu}$	(13)
$\frac{\partial Re}{\partial U_{ref}}$	$\frac{H\rho}{\mu}$	(13)
$\frac{\partial Re}{\partial \mu}$	$-\frac{U_{ref} H \rho}{\mu^2}$	(13)

A summary of all the assumptions made throughout the uncertainty quantification performed in the framework of this research is given in Table 2 along with their purpose.

More details are now given for the uncertainty ϵ_p, pertaining to the FCO432 differential pressure transmitter (Furness Controls Ltd, ±150 Pa) which was used to measure the free-stream dynamic pressure as well as to calibrate the hot-film (uncertainty $\epsilon_{U_{clb}}$ of Eq. 14). This calculation is based on the pressure transducer's manual that can be found in Furness Controls Ltd (2025). This manual contains expressions quantifying three main types of uncertainty: (a) standard uncertainty at 20 °C, (b) long term drift (0.2% per annum) and (c) uncertainty due to temperature difference from the standard temperature of 20 °C. All the types of uncertainties are expressed as percentages of the measured value of the pressure. In this way, the uncertainties ϵ_p and $\epsilon_{U_{clb}}$ (Eq. 18) have been calculated for each measured value. Note that other sources of uncertainty, e.g. due to misalignment of the Pitot-static tube, have not been considered here.

Regarding the calculation of the uncertainty of the hot-film measurements, the computation of $\epsilon_{U_{clb}}$ related to the calibrator (Jørgensen 2001) has already been described (Eq. 18). The uncertainty ϵ_{ft} quantifies the quality of the fit between the calibration points (measured in volts) and the curve representing their correspondence to velocity (in m/s). This error is at most 2% as already mentioned in Sect. 2.4. Finally, the standard uncertainty ϵ_{st} is quantified (similar to what has been already done for the PTV results through Eqs. 6 and 7), as recommended by Bruun (1995). For the time-averaged velocity, the standard uncertainty is calculated through Eq. (6). However, the number of independent samples N_{HF} should be evaluated. This is done through the

Table 2 Summary of all assumptions made throughout the uncertainty quantification procedure presented in Sect. 2.4

Assumption	Purpose
#independent samples = #vortex turnovers	see Eqs. (6), (7), (8)
Covariances of individual velocity components negligible	see Eq. (8)
$\epsilon_{Q_{Re_I}}, \epsilon_{Q_{Re_J}}$ uncorrelated	see Eq. (5)
Uncertainty of barometric pressure (P) negligible	calculation of ϵ_ρ (Eq. 17)
p, ρ uncorrelated (incompressible flow)	calculation of $\epsilon_{U_{ref}}$ or $\epsilon_{U_{clb}}$ (Eq. 18 or 14)
U_{ref}, ρ, μ uncorrelated	calculation of ϵ_{Re} (Eq. 13)
H uncertainty negligible	calculation of ϵ_{Re} (Eq. 13)

following equation (Bruun 1995):

$$N_{HF} \approx \frac{T}{2T_I} \tag{19}$$

where T is the acquisition time and T_I is the integral time scale. Then by applying Eq. (14), ϵ_{HF} can be found for any measured, time-averaged velocity. The normalised version of ϵ_{HF} corresponds to the error bars shown in Figs. 3a and 4a.

By considering that $\sqrt{u'^2} \approx \sigma_U$, then the following equation can be utilised to quantify the standard uncertainty $\epsilon_{\sqrt{u'^2}}$ (Sciacchitano and Wieneke 2016):

$$\epsilon_{\sqrt{u'^2}} = \frac{\sigma_U}{\sqrt{2(N_{HF}-1)}} \tag{20}$$

where σ_U is the standard deviation of the velocity measured by the hot film at a certain position. The normalised version of the latter uncertainty corresponds to the error bars shown in Figs. 3b and 4b.

Finally, a simple numerical example is included here to demonstrate how the measured velocity differences between different Re numbers could translate into mean pressure differences, which could in turn affect wind load estimations. In particular, by considering that Re-independence is observed for the pressure, the scaling law $p \propto \rho U^2$ should hold, where U is a reference velocity. If Re-independence is observed, then this velocity can be selected at any desired position. With the existence of a velocity difference ΔU due to Re-effects, the aforementioned scaling law becomes:

$$p \propto \rho\,(U+\Delta U)^2 = \rho U^2 + 2\rho U \Delta U + \rho\,(\Delta U)^2 = \rho U^2 + \Delta p \tag{21}$$

Hence, in the simplified framework presented above, the mean pressure difference induced by scale effects observed for the velocities is $\Delta p = 2\rho U \Delta U + \rho\,(\Delta U)^2$. An indicative numerical implementation of the equation for Δp could be accomplished by assuming: (i) $U = U_c = 0.3U_{ref}$ (Eq. 1) and (ii) a net difference $E_U = |\Delta U| = \Delta U = 0.1U_{ref}$ (see Sect. 4) with no measurement uncertainty, i.e. $\epsilon_{|\Delta U|} \approx 0$ (Eq. 9). The latter assumption leads to a conservative calculation of Δp, since in reality a net difference of $0.1U_{ref}$, which was encountered on various occasions in this study as already mentioned, would have originated from a higher $|\Delta U|$, when the actual, non-zero measurement uncertainty, $\epsilon_{|\Delta U|}$, is taken into account. Finally, it is derived that $\Delta p/(\rho U_{ref}^2) = 7\%$. As an example, for $Re = 57000$ (i.e. $U_{ref} = 6.25$ m/s) the pressure difference is $\Delta p = 3.3$ Pa while the corresponding pressure uncertainty at 20°C (using an FCO432 differential pressure transmitter) for $p = 1/2\rho U_c$ is $\pm 0.075 Pa$. Therefore, this is an additional indication that the velocity scale effects found in this work cannot be neglected.

Acknowledgements The publication of the article in OA mode was financially supported by HEAL-Link. The authors would also like to acknowledge Dr. Vasiliki Pappa for her help with the calculation of the uncertainty of the hot-wire measurements and Konstantinos Kellaris for his input regarding the passive grid.

Author Contributions N.P.P., B.D., C.G., A.S., and D.B. jointly conceptualised the study. N.P.P. and B.D. conducted the experiments and processed the raw data. C.G., A.S., and D.B. supervised the work. N.P.P. and D.B. developed the data analysis method, which was applied by N.P.P. All authors contributed to the interpretation of the results. N.P.P. wrote the original draft of the manuscript. C.G., A.S., and D.B. reviewed and revised the manuscript. All authors read and approved the final manuscript.

Funding Open access funding provided by HEAL-Link Greece. Partial financial support was received from the European Union, under the research project (PR 101079125) TWEET-IE: Twin Wind tunnels for Energy and the EnvironmenT - Innovations and Excellence.

Data Availability The processed dataset generated during this study is available in Zenodo (DOI: 10.5281/zenodo.15847723).

Declarations

Conflict of interest The authors declare that they have no conflict of interest.

References

Agüera N, Cafiero G, Astarita T et al (2016) Ensemble 3D PTV for high resolution turbulent statistics. Meas Sci Technol 27(12):124011. https://doi.org/10.1088/0957-0233/27/12/124011

Ahn S, Fessler JA (2003) Standard errors of mean, variance, and standard deviation estimators. EECS Department, The University of Michigan 1(2). https://www.eecs.umich.edu/techreports/systems/cspl/cspl-413.pdf

Ai Z, Mak CM (2017) CFD simulation of flow in a long street canyon under a perpendicular wind direction: evaluation of three computational settings. Build Environ 114:293–306. https://doi.org/10.1016/j.buildenv.2016.12.032

American Society of Civil Engineers (2012) Wind tunnel testing for buildings and other structures. Am Soc CivilEng. https://doi.org/10.1061/9780784412282

Bady M, Kato S, Takahashi T et al (2011) An experimental investigation of the wind environment and air quality within a densely populated urban street canyon. J Wind Eng Ind Aerodyn 99(8):857–867. https://doi.org/10.1016/j.jweia.2011.06.005

Bhattacharya S, Vlachos PP (2020) Volumetric particle tracking velocimetry (PTV) uncertainty quantification. Exp Fluids 61(9):197. https://doi.org/10.1007/s00348-020-03021-6

Blackman K, Perret L, Savory E (2015) Effect of upstream flow regime on street canyon flow mean turbulence statistics. Environ Fluid Mech 15(4):823–849. https://doi.org/10.1007/s10652-014-9386-8

Blackman K, Perret L, Mathis R (2019) Assessment of inner-outer interactions in the urban boundary layer using a predictive model. J Fluid Mech 875:44–70. https://doi.org/10.1017/jfm.2019.427

Bruun H (1995) Hot-wire anemometry: principles and signal analysis. Oxford science publications, Oxford University Press, Oxford

Castro I, Robins A (1977) The flow around a surface-mounted cube in uniform and turbulent streams. J Fluid Mech 79(2):307–335. https://doi.org/10.1017/S0022112077000172

Cheng C, Fu C (2010) Characteristic of wind loads on a hemispherical dome in smooth flow and turbulent boundary layer flow. J Wind Eng Ind Aerodyn 98(6–7):328–344. https://doi.org/10.1016/j.jweia.2009.12.002

Chew LW, Norford LK (2018) Pedestrian-level wind speed enhancement in urban street canyons with void decks. Build Environ 146:64–76. https://doi.org/10.1016/j.buildenv.2018.09.039

Chew LW, Aliabadi AA, Norford LK (2018) Flows across high aspect ratio street canyons: Reynolds number independence revisited. Environ Fluid Mech 18:1275–1291. https://doi.org/10.1007/s10652-018-9601-0

Cui PY, Li Z, Tao WQ (2014) Investigation of Re-independence of turbulent flow and pollutant dispersion in urban street canyon using numerical wind tunnel (NWT) models. Int J Heat Mass Transf 79:176–188. https://doi.org/10.1016/j.ijheatmasstransfer.2014.07.096

Cui PY, Chen WQ, Wang JQ et al (2022) Numerical studies on issues of Re-independence for indoor airflow and pollutant dispersion within an isolated building. Build Simul 15(7):1259–1276. https://doi.org/10.1007/s12273-021-0846-z

Del Ponte AV, Fellini S, Marro M et al (2024) Influence of street trees on turbulent fluctuations and transport processes in an urban canyon: a wind tunnel study. Bound-Layer Meteorol 190(2):6. https://doi.org/10.1007/s10546-024-00875-9

Dsouza B, Sciacchitano A, Yu W (2024) Reynolds Number Independence In An Urban Street Canyon Using 3D Robotic Particle Tracking Velocimetry. In: 21st International Symposium on the Application of Laser and Imaging Techniques to Fluid Mechanics, LISBON Simposia, p 171, https://doi.org/10.55037/lxlaser.21st.171

Faleiros DE, Tuinstra M, Sciacchitano A et al (2018) Helium-filled soap bubbles tracing fidelity in wall-bounded turbulence. Exp Fluids 59(3):56. https://doi.org/10.1007/s00348-018-2502-7

Faleiros DE, Tuinstra M, Sciacchitano A et al (2019) Generation and control of helium-filled soap bubbles for PIV. Exp Fluids 60(3):40. https://doi.org/10.1007/s00348-019-2687-4

Furness Controls Ltd. (2025) FCO432 Pressure Transducer. https://www.furness-controls.com/product/fco432/, accessed: 24 Feb 2026

Gromke C, Ruck B (2007) Influence of trees on the dispersion of pollutants in an urban street canyon-experimental investigation of the flow and concentration field. Atmos Environ 41(16):3287–3302. https://doi.org/10.1016/j.atmosenv.2006.12.043

Gromke C, Ruck B (2009) On the impact of trees on dispersion processes of traffic emissions in street canyons. Bound-Layer Meteorol 131:19–34. https://doi.org/10.1007/s10546-008-9301-2

Gromke C, Buccolieri R, Di Sabatino S et al (2008) Dispersion study in a street canyon with tree planting by means of wind tunnel and numerical investigations-evaluation of CFD data with experimental data. Atmos Environ 42(37):8640–8650. https://doi.org/10.1016/j.atmosenv.2008.08.019

Hölling M, Wagner M, Bocarov E et al (2025) Round-Robin test II–wake measurements of porous discs under clearly defined boundary conditions. J Phys: Conf Ser 3016(1):012013. https://doi.org/10.1088/1742-6596/3016/1/012013

Hunter LJ, Watson I, Johnson G (1990) Modelling air flow regimes in urban canyons. Energy Build 15(3–4):315–324. https://doi.org/10.1016/0378-7788(90)90004-3

Janke T, Michaelis D (2021) Uncertainty quantification for PTV/LPT data and adaptive track filtering. 14th international symposium on particle image velocimetry. https://doi.org/10.18409/ispiv.v1i1.125

Jaroslawski T, Perret L, Blackman K et al (2019) The spanwise variation of roof-level turbulence in a street-canyon flow. Bound-Layer Meteorol 170(3):373–394. https://doi.org/10.1007/s10546-018-0405-z

Jeong SJ, Andrews MJ (2002) Application of the k-ε turbulence model to the high Reynolds number skimming flow field of an urban street canyon. Atmos Environ 36(7):1137–1145. https://doi.org/10.1016/S1352-2310(01)00569-6

Jørgensen FE (2002) How to measure turbulence with hot-wire anemometers: a practical guide.(Dantec dynamics)

Jux C, Sciacchitano A, Schneiders JF et al (2018) Robotic volumetric PIV of a full-scale cyclist. Exp Fluids 59(4):74. https://doi.org/10.1007/s00348-018-2524-1

Kastner-Klein P, Berkowicz R, Britter R (2004) The influence of street architecture on flow and dispersion in street canyons. Meteorol Atmos Phys 87(1):121–131. https://doi.org/10.1007/s00703-003-0065-4

Kellnerová R, Kukačka L, Jurčáková K et al (2012) PIV measurement of turbulent flow within a street canyon: detection of coherent motion. J Wind Eng Ind Aerodyn 104–106:302–313. https://doi.org/10.1016/j.jweia.2012.02.017

Kim D, Kim M, Saredi E et al (2020) Robotic PTV study of the flow around automotive side-view mirror models. Exp Therm Fluid Sci 119:110202. https://doi.org/10.1016/j.expthermflusci.2020.110202

Kistler A, Vrebalovich T (1966) Grid turbulence at large Reynolds numbers. J Fluid Mech 26(1):37–47. https://doi.org/10.1017/s0022112066001071
Li XX, Liu CH, Leung DY et al (2006) Recent progress in CFD modelling of wind field and pollutant transport in street canyons. Atmos Environ 40(29):5640–5658. https://doi.org/10.1016/j.atmosenv.2006.04.055
Li XX, Leung DY, Liu CH et al (2008) Physical Modeling of Flow Field inside Urban Street Canyons. J Appl Meteorol Climatol 47(7):2058–2067. https://doi.org/10.1175/2007JAMC1815.1
Lim HC, Castro IP, Hoxey RP (2007) Bluff bodies in deep turbulent boundary layers: Reynolds-number issues. J Fluid Mech 571:97–118. https://doi.org/10.1017/S0022112006003223
Lin Y, Hang J, Yang H et al (2021) Investigation of the Reynolds number independence of cavity flow in 2D street canyons by wind tunnel experiments and numerical simulations. Build Environ 201:107965. https://doi.org/10.1016/j.buildenv.2021.107965
Memon RA, Leung D (2011) On the heating environment in street canyon. Environ Fluid Mech 11(5):465–480. https://doi.org/10.1007/s10652-010-9202-z
Meroney RN, Pavageau M, Rafailidis S et al (1996) Study of line source characteristics for 2-D physical modelling of pollutant dispersion in street canyons. J Wind Eng Ind Aerodyn 62(1):37–56. https://doi.org/10.1016/s0167-6105(96)00057-8
Mirzaei PA, Haghighat F (2011) Pollution removal effectiveness of the pedestrian ventilation system. J Wind Eng Ind Aerodyn 99(1):46–58. https://doi.org/10.1016/j.jweia.2010.10.007
Oke TR (1988) Street design and urban canopy layer climate. Energy Build 11(1–3):103–113. https://doi.org/10.1016/0378-7788(88)90026-6
Pallas NP, Dsouza B, Pappa V (2025) Twin test 4 of TWEET-IE project: Scale effects on the flow in an urban street canyon. Zenodo, PTV data from wind tunnel experiments at NTUA and TU Delft. https://doi.org/10.5281/zenodo.15847723
Pavageau M, Schatzmann M (1999) Wind tunnel measurements of concentration fluctuations in an urban street canyon. Atmos Environ 33(24–25):3961–3971. https://doi.org/10.1016/S1352-2310(99)00138-7
Raffel M, Willert CE, Scarano F et al (2018) Particle image velocimetry: a practical guide. Springer. https://doi.org/10.1007/978-3-319-68852-7
Richards P, Hoxey R, Short L (2001) Wind pressures on a 6 m cube. J Wind Eng Ind Aerodyn 89(14–15):1553–1564. https://doi.org/10.1016/s0167-6105(01)00139-8
Roach P (1987) The generation of nearly isotropic turbulence by means of grids. Int J Heat Fluid Flow 8(2):82–92. https://doi.org/10.1016/0142-727x(87)90001-4
Rotello CM, Myers JL, Well AD, et al (2025) Research Design and Statistical Analysis, 4th edn. Routledge, New York, https://doi.org/10.4324/9781003453550
Salizzoni P, Soulhac L, Mejean P (2009) Street canyon ventilation and atmospheric turbulence. Atmos Environ 43(32):5056–5067. https://doi.org/10.1016/j.atmosenv.2009.06.045
Salizzoni P, Marro M, Soulhac L et al (2011) Turbulent transfer between street canyons and the overlying atmospheric boundary layer. Bound-Layer Meteorol 141(3):393–414. https://doi.org/10.1007/s10546-011-9641-1
Savory E, Perret L, Rivet C (2013) Modelling considerations for examining the mean and unsteady flow in a simple urban-type street canyon. Meteorol Atmos Phys 121(1):1–16. https://doi.org/10.1007/s00703-013-0254-8
Scarano F, Ghaemi S, Caridi GCA et al (2015) On the use of helium-filled soap bubbles for large-scale tomographic PIV in wind tunnel experiments. Exp Fluids 56(2):42. https://doi.org/10.1007/s00348-015-1909-7
Schanz D, Schröder A, Gesemann S, et al (2013) 'Shake The Box': A highly efficient and accurate Tomographic Particle Tracking Velocimetry (TOMO-PTV) method using prediction of particle positions. In: PIV13; 10th International Symposium on Particle Image Velocimetry, Delft, The Netherlands, July 1-3, 2013, Delft University of Technology, The Faculty of Mechanical, Maritime and Materials Engineering, https://repository.tudelft.nl/file/File_87f9b03e-30d1-4626-9053-0a462afc1d33?preview=1
Schanz D, Gesemann S, Schröder A (2016) Shake-The-Box: Lagrangian particle tracking at high particle image densities. Exp Fluids 57:1–27. https://doi.org/10.1007/s00348-016-2157-1
Schneiders JF, Sciacchitano A (2017) Track benchmarking method for uncertainty quantification of particle tracking velocimetry interpolations. Meas Sci Technol 28(6):065302. https://doi.org/10.1088/1361-6501/aa6a03
Schneiders JF, Scarano F, Jux C et al (2018) Coaxial volumetric velocimetry. Meas Sci Technol 29(6):065201. https://doi.org/10.1088/1361-6501/aab07d
Sciacchitano A (2019) Uncertainty quantification in particle image velocimetry. Meas Sci Technol 30(9):092001. https://doi.org/10.1088/1361-6501/ab1db8
Sciacchitano A, Wieneke B (2016) PIV uncertainty propagation. Meas Sci Technol 27(8):084006. https://doi.org/10.1088/0957-0233/27/8/084006
Shu C, Wang LL, Mortezazadeh M (2020) Dimensional analysis of Reynolds independence and regional critical Reynolds numbers for urban aerodynamics. J Wind Eng Ind Aerodyn 203:104232. https://doi.org/10.1016/j.jweia.2020.104232
Snyder WH (1981) Guideline for fluid modeling of atmospheric diffusion, vol 81. Environmental Protection Agency, Environmental Sciences Research Laboratory, Office of Research and Development, U.S
(2007) Wind effects on buildings and design of wind-sensitive structures. Springer Vienna. https://doi.org/10.1007/978-3-211-73076-8
Suzuki T, Sanse A, Mizushima T et al (2009) Unsteady PTV velocity field past an airfoil solved with DNS: Part 2. validation and application at Reynolds numbers up to $Re \leq 10^4$. Exp Fluids 47(6):977–994. https://doi.org/10.1007/s00348-009-0692-8
Timmins BH, Wilson BW, Smith BL et al (2012) A method for automatic estimation of instantaneous local uncertainty in particle image velocimetry measurements. Exp Fluids 53(4):1133–1147. https://doi.org/10.1007/s00348-012-1341-1
Uehara K, Wakamatsu S, Ooka R (2003) Studies on critical Reynolds number indices for wind-tunnel experiments on flow within urban areas. Bound-Layer Meteorol 107(2):353–370. https://doi.org/10.1023/A:1022162807729
VDI 3783 Part 12 (2000) Environmental meteorology: physical modelling of flow and dispersion processes in the atmospheric boundary layer. Beuth Verlag, Berlin, Applications of Wind Tunnels
Vita G, Hemida H, Andrianne T et al (2018) Generating atmospheric turbulence using passive grids in an expansion test section of a wind tunnel. J Wind Eng Ind Aerodyn 178:91–104. https://doi.org/10.1016/j.jweia.2018.02.007
White FM (2006) Viscous fluid flow, 3rd edn. McGraw-Hill Higher Education, Boston, MA
Wieneke B (2008) Volume self-calibration for 3D particle image velocimetry. Exp Fluids 45(4):549–556. https://doi.org/10.1007/s00348-008-0521-5
Wu YP, Cui PY, Wang KX et al (2025) A numerical study on the issue of Reynolds independence of flow and dispersion within isolated street canyons. Build Environ 267:112202. https://doi.org/10.1016/j.buildenv.2024.112202
Xie X, Liu CH, Leung DY (2007) Impact of building facades and ground heating on wind flow and pollutant transport in street

canyons. Atmos Environ 41(39):9030–9049. https://doi.org/10.1016/j.atmosenv.2007.08.027

Xue Y, Zhao Y, Mei SJ et al (2024) Exploring thermal buoyant flow in urban street canyons: influence of approaching turbulent boundary layer. Exp Therm Fluid Sci 158:111255. https://doi.org/10.1016/j.expthermflusci.2024.111255

Xue Y, Zhao Y, Mei SJ et al (2024) Impact of street canyon morphology on heat and fluid flow: an experimental water tunnel study using simultaneous PIV-LIF technique. Exp Therm Fluid Sci 150:111066. https://doi.org/10.1016/j.expthermflusci.2023.111066

Zajic D, Fernando HJS, Calhoun R et al (2011) Flow and turbulence in an urban canyon. J Appl Meteorol Climatol 50(1):203–223. https://doi.org/10.1175/2010JAMC2525.1

Zhao Y, Li H, Kubilay A et al (2021) Buoyancy effects on the flows around flat and steep street canyons in simplified urban settings subject to a neutral approaching boundary layer: Wind tunnel PIV measurements. Sci Total Environ 797:149067. https://doi.org/10.1016/j.scitotenv.2021.149067

Zhu S, Chew LW (2025) Flows across 3D Urban street canyons: revisiting Reynolds number independence by large eddy simulation. Build Environ 285:113635. https://doi.org/10.1016/j.buildenv.2025.113635